https://doi.org/10.5194/egusphere-2026-4830
Preprint. Discussion started: 20 August 2026

Uncertainty in an Adapted Analytic CO_2 Flux Inversion Model ($AACO_2FIM$) under different spatiotemporal coverages

Pingping Rong[1] and Hui Su[1]

1. State Key Laboratory of Climate Resilience for Coastal Cities, Department of Civil and Environmental Engineering, the Hong Kong University of Science and Technology, Clear Water Bay, Hong Kong SAR, China

Correspondence to: Pingping Rong (pprong@ust.hk) and Hui Su (cehsu@ust.hk)

Abstract. We developed an Adapted Analytic CO_2 Flux Inversion Model ($AACO_2FIM$) by adapting the Integrated Methane Inversion system for CO_2 applications. We applied $AACO_2FIM$ to examine how closely the regulated solution aligns with predefined emission variability patterns described by target scaling factors (SFs) used to generate pseudo-observations, thereby isolating uncertainty arising solely from cost-function minimization under the quasi-linear assumption. To concurrently assess spatiotemporal coverage impacts, we revised the inversion package to incorporate two different coverage configurations: Orbiting Carbon Observatory-2 (OCO-2) tracks (oco2Trks) and an hourly global grid (FullC).

Inversion performance was quantified by the convergence of inverted SFs toward target SFs under varying prior-target mismatches and observational coverages over an 8-day window following a one-month spinup. The ensemble-mean posterior SFs reproduced the target patterns, with convergence controlled by forward-model sensitivity and observational coverage. Baseline cases showed near-exact convergence, whereas larger prior-target differences led to poorer convergence. The oco2Trks inversions produced a shrunk but highly correlated valid inversion domain relative to FullC, and both configurations showed the largest posterior variability coinciding with the highest forward-model sensitivity. Under oco2Trks (<10% coverage of FullC), the observation-related cost function term required a weight two orders of magnitude larger than that of FullC to achieve the best fit quality. When OCO-2 observations were used as a constraint, the inverted SF variability generally matched the bias patterns between forward-modeled concentrations and OCO-2 measurements.

1. Introduction

Over the past several decades, top-down flux inversion has been the focus of intense study, particularly as reducing carbon emissions to mitigate climate change and improve air quality has become a global priority. Ground-based and satellite measurements, along with land-ocean-atmosphere model outputs, are systematically integrated to achieve more accurate flux inversion. Significant efforts have been made to improve the accuracy of bottom-up emission inventories, develop versatile inversion algorithms, and establish a multi-satellite observational network for conducting these inversions. Reducing uncertainties in all components of the modeling and observational system is essential for accurate carbon-flux estimates.

https://doi.org/10.5194/egusphere-2026-4830
Preprint. Discussion started: 20 August 2026

Despite major progress over the years (e.g., Ciais et al., 2010; Kondo et al., 2015, 2020; Hu et al., 2024), significant uncertainties persist due to the highly complex nature of the carbon cycle, a lack of observations, and modeling limitations.

Additionally, local demand for high-resolution regional inverted fields for specific time frames cannot be fully met through general advances in the modeling community. Regional models need coarser-grid global inversions for the same time frames to be readily available, highlighting the need for long-term maintenance of both global and regional models chosen by the local community. A comprehensive uncertainty analysis—tailored to the specific models and observations in use—must be conducted; otherwise, the inversion results may have limited applicability.

Atmospheric minor-constituent flux inversion refers to an algorithm that minimizes a Bayesian cost function to obtain an optimal posterior emission scaling factor (SF) given a transport model and observed concentration fields over a specified time frame. The cost function J is the sum of two terms:

emission-related term-1: $(\mathbf{x}-\mathbf{x}_\mathrm{a})^\mathrm{T}\mathbf{S}_\mathrm{a}^{-1}(\mathbf{x}-\mathbf{x}_\mathrm{a})$ (1)

and the concentration-related term-2: $\gamma(\mathbf{y}-\mathbf{K}\mathbf{x})^\mathrm{T}\mathbf{S}_\mathrm{o}^{-1}(\mathbf{y}-\mathbf{K}\mathbf{x})$ (2)

Here, $\mathbf{K} = \partial\mathbf{y}/\partial\mathbf{x}$ is the Jacobian matrix; $\mathbf{S}_\mathrm{a}$ is the prior error covariance matrix; $\mathbf{S}_\mathrm{o}$ is the observational error covariance matrix; and coefficient γ adjusts the relative weight of the two terms. The variables $\mathbf{x}$ and $\mathbf{y}$ denote SFs and concentrations, with $\mathbf{x}$ spanning the state-vector space (individual or aggregated spatial pixels) and y spanning the spatiotemporal observation space.

In term-1, the SF covariance matrix is scaled by the prior error (expressed as a percentage). In term-2, the covariance matrix of the concentration differences is scaled by the observational error. The Jacobian matrix ($\mathbf{K}$) describes the transport-model-constrained relationship between the emission SF and the concentration fields, indicating the sensitivity of concentration changes to given changes in the SF.

Minimizing the Bayesian cost function can be done either iteratively (variational methods) (e.g., Liu et al., 2014) or analytically under a quasi-linearity assumption, as in IMI (Varon et al., 2022). The analytical solution is obtained by setting $\mathrm{d}J/\mathrm{d}\mathbf{x} = 0$, yielding posterior SFs in the state-vector space:

$$\hat{\mathbf{x}} = \mathbf{x}_\mathrm{a} + (\gamma\mathbf{K}^\mathrm{T}\mathbf{S}_\mathrm{o}^{-1}\mathbf{K} + \mathbf{S}_\mathrm{a}^{-1})^{-1}\gamma\mathbf{K}^\mathrm{T}\mathbf{S}_\mathrm{o}^{-1}(\mathbf{y}-\mathbf{K}\mathbf{x}_\mathrm{a}) \quad (3)$$

which shows explicitly how the prior $\mathbf{x}_\mathbf{a}$ and the observations $\mathbf{y}$ are combined to yield the posterior $\hat{\mathbf{x}}$, with γ controlling the relative weight of the observations. Physical constraints (for example, enforcing non-negativity of $\hat{\mathbf{x}}$, not shown here) can be imposed by reformulating the cost function (e.g., applying a logarithmic transform to $\hat{\mathbf{x}}$ and $\mathbf{x}_\mathbf{a}$); however, such adjustments can alter the problem's stochastic structure and thus affect posterior uncertainty estimates (Miller et al., 2014; Maasakkers et al., 2019).

https://doi.org/10.5194/egusphere-2026-4830
Preprint. Discussion started: 20 August 2026

In this study, we replaced methane (CH_4) with carbon dioxide (CO_2) to perform inversions using the Integrated Methane Inversion (IMI) framework. Besides model development, the paper aims to assess uncertainty in the inverted emission scaling factor (SF) under both full global coverage (5° longitude × 4° latitude) and the Orbiting Carbon Observatory-2 (OCO-2) coverage. This assessment uses a series of prior-disturbance and pseudo-observation designs. Section 2 describes the modifications made to the model components to carry out the CO_2 inversion, the model setup, and experimental design. Section 3 details the datasets used as model inputs. Model spin-up analysis is presented in Section 4. Section 5 presents the inversion results for all cases and examines the γ-dependency last. Section 6 provides discussion and conclusions.

2. Models and setup

2.1. IMI review

Varon et al. (2022) provide a step-by-step overview of the IMI model package. IMI is an open-access, cloud-based facility that enables users to estimate methane emissions for selected regions of interest by performing high-resolution (0.25° latitude × 0.3125° longitude) analytical inversions of TROPOspheric Monitoring Instrument (TROPOMI) satellite data archived in the cloud, with error characterization included in the inversion results. The forward transport model in IMI is GEOS-Chem, an open-access community model that simulates a large list of the atmospheric trace gases, and is driven by meteorological fields from NASA's Goddard Earth Observing System (GEOS). Using a similar high-resolution configuration, Shen et al. (2022) applied IMI to CH_4 flux inversions across major emission domains on all continents to compare inverted corrections with inventory emissions.

Both analytic and variational inversions use the constraint $dJ/d\mathbf{x} = 0$. Variational methods are commonly used in numerical weather prediction to optimize meteorological fields; here they are applied to optimize a 2D emission field and a 3D concentration field (Meirink et al., 2008). The variational approach uses an adjoint model to compute the cost-function gradient, and updates each state-vector element iteratively along the steepest-descent direction. Many iterations (e.g., ~70 in Liu et al., 2013; ~50 in Niwa et al., 2022; Polavarapu, 2004) can be costly because each iteration requires both forward and adjoint model runs. Analytical solutions exploit the quasi-linearity between emission changes and concentration responses but require explicit construction of the Jacobian matrix **K** for all state-vector elements, which can also be time-consuming. However, computational cost drops substantially for shorter time windows and coarser resolution. If the sensitivity is poor for a given element, the inversion for that element becomes ineffective.

2.2. Components changed in IMI for the CO_2 inversion

In the GEOS-Core for CO_2, we incorporated a state vector $\hat{\mathbf{x}}$ to store the inverted SF field. For the experiments here, $\hat{\mathbf{x}}$ has 3,358 elements (73 longitudes × 46 latitudes). An IMI preview using OCO-2 orbital tracks showed degrees of freedom (DOFs) ≈ 60—far fewer than the 3,358 state elements. The estimated DOF for a pixel depends on the number of measurements in that pixel: it approaches 1.0 with many measurements and is zero with none. Nonetheless, we chose not to apply the aggregation

https://doi.org/10.5194/egusphere-2026-4830
Preprint. Discussion started: 20 August 2026

routine to reduce the number of state vector elements for several reasons. First, aggregation can introduce errors (Jacob et al., 2016) and may obscure pixel-level variability we wish to resolve. Second, using full spatiotemporal coverage allows DOFs reach their maximum capacity of 3,358.

As needed, we integrated emission-perturbation and emission-scaling-factor capabilities into the GEOS-Core to develop a code package for the CO_2 inversion. Observation and transport-related concentration errors were set at 4.0 ppm and 1.0 ppm, respectively, and the prior uncertainty of $\mathbf{x_a}$ was set to 50%, mirroring the cloud-based IMI settings. These error choices are simplified because our main goal is to test how well the inversion reproduces the target SFs corresponding to the pseudo-observations, rather than to produce correction SFs for real emissions. We run a 1-month spin-up in January 2019, followed by an inversion period from 1 February to 8 February.

2.3. Experiment design

2.3.1. Prior emission SFs for ensemble runs

We used perturbed prior emission scaling factors (SFs) in ensemble runs to remove the nonlinearity in the inverted field especially near coasts, to avoid singularities issue in the analytic inversion, and to explore different emission-forcing regimes. Two disturbance types were applied to the prior emissions: random noise and a longitudinal wave-1 sinusoid with random phase. The wave-1 pattern was chosen to mimic larger or smaller emissions across broad regions (e.g., the Americas, Europe, or China). Prior emissions were derived from bottom-up inventories (see Section 3.1).

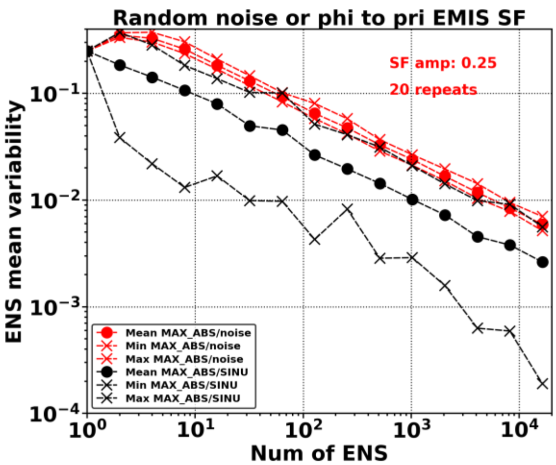

Figure 1: Demonstration of how the ensemble mean of 2D perturbation fields approaches zero systematically as a function of ensemble size (Num of ENS). For the black curves, Num of ENS random noise fields were generated, each uniformly distributed in the range [-0.25, 0.25] across 3,358 state vector elements (pixels). For the red curves, Num of ENS wave-1 fields were generated, each with a random phase uniformly distributed between [0°, 360°]. For both the black and red curves, the largest deviation from zero (MAX_ABS) is extracted from the ensemble mean field (across 3,358 pixels). Twenty independent repetitions were performed to obtain the maximum, mean, and minimum values of MAX_ABS.

For each state-vector element, we aim for the ensemble sum of prior emission disturbances to approach zero. Figure 1 shows

https://doi.org/10.5194/egusphere-2026-4830
Preprint. Discussion started: 20 August 2026

that the summed SF disturbances decrease continuously for both random and wave-1 disturbances (amplitude 0.25) as ensemble size grows. To reduce computational cost, we used only 2–3 ensembles and enforced a zero mean per pixel. We call the SF field that generates the pseudo-observation concentrations the target emission SF field. Using a small set of prior SFs together with the known target enables us to clearly see how the ensemble mean differs from each prior, demonstrating how inverted SFs behave across cases. However, a small ensemble can fail to remove features arising from local nonlinear responses—for example, if one prior member closely matches the target while others do not, the nonlinearity can be highlighted.

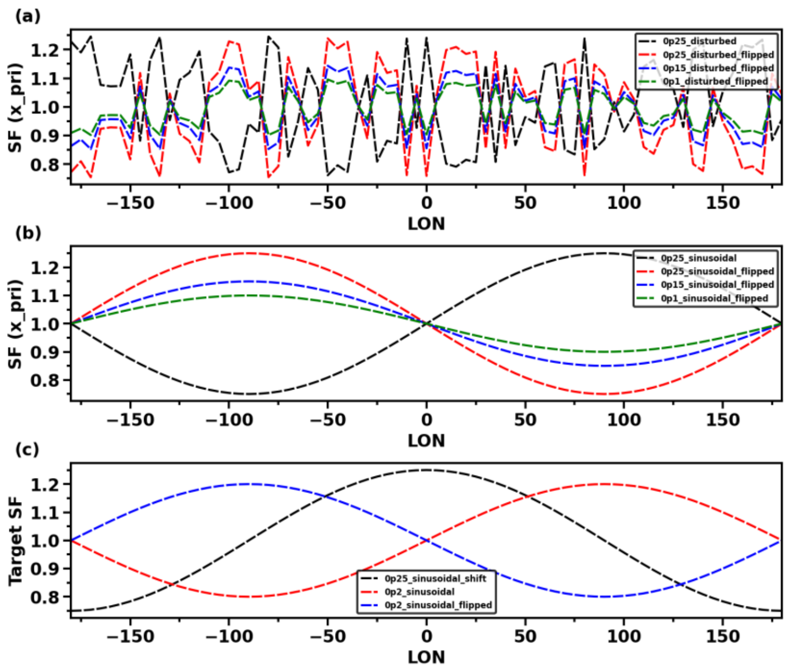

Figure 2: (a) Longitudinal cross-section of random noise as the chosen prior SF perturbation, for demonstration; this includes all components of the disturbed-pair and disturbed-three detailed in the text. In the legend, "0p25" denotes an amplitude of 0.25, while "flipped" refers to the anti-phase counterparts of the black curves. (b) Wave-1 prior SF patterns, including all components of the sinusoidal-pair and sinusoidal-three configurations. Black paired with red constitutes the sinusoidal/disturbed pair, and black, blue, and green constitute the sinusoidal/disturbed three. (c) Wave-1 SF curves (target SFs) used to generate the target concentration fields. Black is T1, red is T2, and blue is T3.

To create disturbed prior SF fields, we first generated a random-noise field and its exact opposite (anti-phase) to form a pair for the two-member ensemble. We then created two additional anti-phase noise fields with amplitudes 1.0 and 1.5, producing a three-member ensemble. A longitudinal cross section of the disturbed noise fields is shown in Figure 2a. The same procedure was applied to sinusoidal disturbances, producing a sinusoidal-pair and a sinusoidal-three, shown in Figure 2b.

2.3.2. Target emission SFs

We created four pseudo-observation spatiotemporal fields with GEOS-Chem. Target zero (T0) used the original total emissions, so its SF is uniformly 1.0. Target one (T1) used a longitudinal wave-1 SF (amplitude 0.25) peaking at 0° longitude. Targets two (T2) and three (T3) used wave-1 SFs with amplitude 0.2, peaking at 90° and -90° longitude, respectively (Figure 2c). We

https://doi.org/10.5194/egusphere-2026-4830
Preprint. Discussion started: 20 August 2026

also included OCO-2 satellite measurements (labeled T_oco2), which have no associated SF. For T0–T3 we used two spatiotemporal coverages: hourly full coverage on a grid of 4° latitude × 5° longitude (FullC) and OCO-2 orbital track coverage (oco2Trks).

We clarify that the regularized solution $\hat{\mathbf{x}}$ is not expected to match the targets (T1, T2, or T3) exactly. However, understanding exactly where it lies relative to the prior and a given target makes the flux inversion process more transparent and less of a "black box." We used the coarsest GEOS-Chem resolution to enable many experiments, as high-resolution global forward runs and inversions are computationally prohibitive. Although the relationship between high- and low-resolution runs are more complex than simple spatial smoothing and may introduce biases (Liu et al., 2024), we expect our conclusions to hold true qualitatively across different resolutions. Further testing can be conducted as needed to verify this.

3. Data downloaded

3.1. Inventories ingested and the HEMCO diagnostics

The Harmonized Emissions Component (HEMCO) is one of two GEOS-Chem components; the other, GEOS-Core, handles chemistry and transport. HEMCO reads and processes emission inventories and interfaces with GEOS-Core to apply emission forcing. In our simulations the activated emission inventories (with their native resolutions and original configuration symbols) are: FOSSIL_ODIAC (1° × 1°), AEIC2019_MONMEAN with AEIC_SCALE_1990_2019 (0.625° × 0.5°), CEDS_SHIP (0.5° × 0.5°), CO2CORR (2.5° × 2°), OCEAN_EXCH_SCALED (5° × 4°), BBIO_SIB3 (1.25° × 1°), and NET_TERR_EXCH (1° × 1°).

Figures 3–4 show the individual contributions and total emissions from the HEMCO diagnostics, labeled with the inversion start date (1 February 2019). When an inventory directly provides global CO_2 fluxes, the HEMCO output closely matches that inventory. In contrast, notable changes can arise when regional inventories are incorporated (not shown). Additionally, low spikes may appear along coastlines (not shown) that are not present in the original inventories, even though we did not observe a significant impact from these spikes on the inversion results.

The Open-source Data Inventory for Anthropogenic CO_2 (ODIAC) covers 2000–2018 on a monthly basis (Oda et al., 2011; Oda et al., 2018). It was generated from point-source emissions and nighttime-light satellite data to map land-based emissions only, excluding gas flaring, shipping, and aviation. Figure 3a shows that fossil-fuel emissions dominate the other contributions, especially over land in the Northern Hemisphere. Eastern China has the highest emissions, corresponding to the peak total emissions in Figure 4a.

The Aviation Emissions Inventory Code (AEIC) quantifies and standardizes aircraft emissions during landing and take-off (LTO) and non-LTO phases (climb, cruise, descent) using code developed at MIT (Kim et al., 2007; Stettler et al., 2011; Simone et al., 2013; Teoh et al., 2024). The AEIC2019 monthly-mean outputs for January and February are on a 0.625° longitude ×

https://doi.org/10.5194/egusphere-2026-4830
Preprint. Discussion started: 20 August 2026

0.5° latitude grid and include 36 vertical layers from the surface to 17.5 km at ~0.5 km intervals, which approximately match GEOS-Chem's lowest 36 layers. The inventory's FUELBURN variable was used as HEMCO input with a scaling factor of

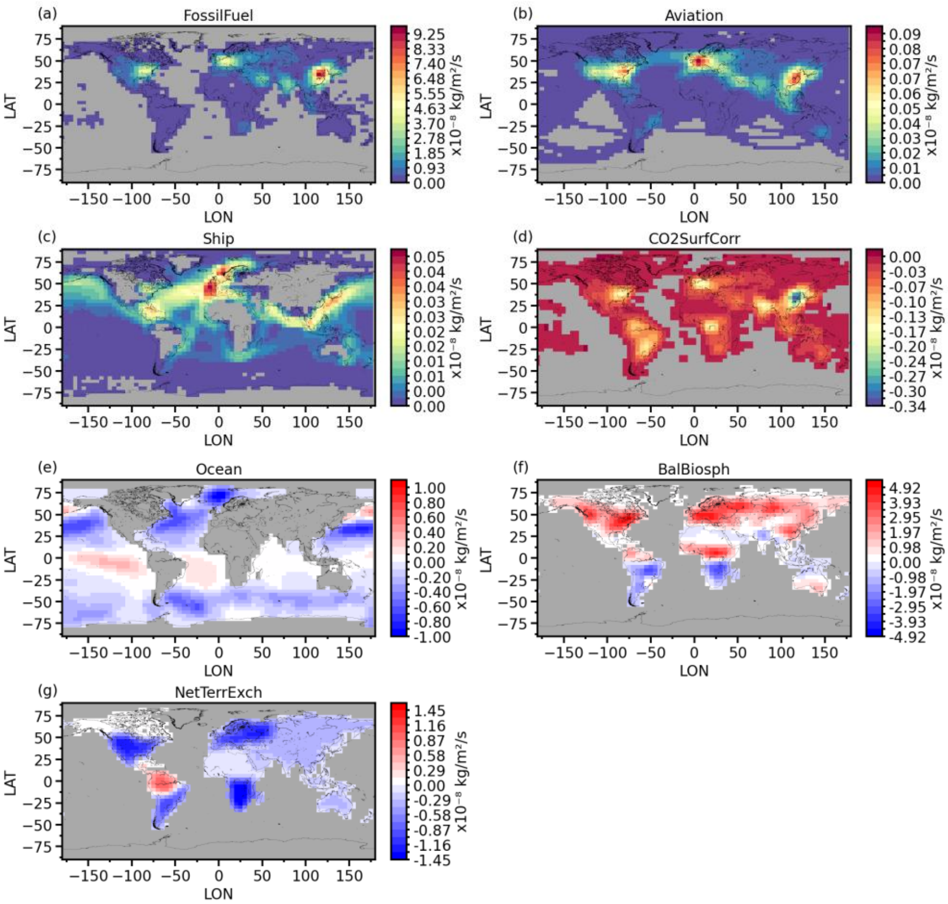

Figure 3: HEMCO CO_2 emissions on 1 February 2019 by individual sector.

1.0. Figure 3b shows that aviation emissions are about 1% of total emissions, with peaks over land in the Northern Hemisphere—notably the United States, Europe, and eastern China.

Ship emissions are sourced from the Community Emissions Data System (CEDS) (Hoesly et al., 2018; Feng et al., 2020). Historical anthropogenic emissions (1750–2019) were mapped to a 0.5° global grid for the Coupled Model Intercomparison Project Phase 6 (CMIP6). Country- and sector-level emissions in CEDS were aggregated into nine final sectors: agriculture, energy, industry, transportation, residential–commercial–other, solvents, waste, international shipping, and aircraft. Figure 3c shows that ship emissions—approximately half of aviation emissions—are particularly significant in the Northwest Pacific, near Europe, the Northeast Atlantic, and globally along coastlines.

https://doi.org/10.5194/egusphere-2026-4830
Preprint. Discussion started: 20 August 2026

Surface correction adjusts emissions to remove CO_2 produced by oxidation of other emitted species (e.g., CH_4, isoprene, monoterpenes). CH_4 sources include 2004 monthly-mean wetland emissions and annual averages for livestock, landfills, rice, and other natural sources (e.g., termites). Isoprene (C5H8) and monoterpenes (C10H16) are tree-emitted biogenic volatile organic compound (BVOCs) (Hantson et al., 2017) that can oxidize to CO_2. These emissions and CO_2 production rates from CO are taken from GEOS5_47L output; note that CO_2 production from CO is handled via CHEMISTRY_INPUT and is not included in the surface correction. Figure 3d shows these corrections peak in several continental regions—particularly eastern China—where they can reach about 3% of total emissions.

The oceans and land biosphere are major CO_2 sinks that substantially reduce the atmospheric CO_2 growth rate from anthropogenic emissions (Crisp et al., 2022). Furthermore, climate change may introduce decadal variability in ocean CO_2 uptake—both open and coastal—through factors such as changes in biological carbon fixation (Mathis et al., 2024). OCEAN_EXCH_SCALED refers to a dataset providing monthly values from 2000–2013 (168 time-frames), using year 2000 as the reference (Takahashi et al., 2009). The net sea–air CO_2 flux is calculated as ΔpCO_2 (surface water pCO_2 minus atmospheric pCO_2 for 2000) multiplied by the gas transfer coefficient, with the air–sea transfer rate parameterized as a function of wind speed squared. Figure 3e shows a slightly positive flux near the equator but is predominantly negative overall, indicating net ocean CO_2 uptake; the strongest uptake reaches about 10% of total emissions.

Net ecosystem exchange (NEE) has two components. The first is balanced biosphere fluxes, which include natural non-respiratory carbon losses from the biosphere (e.g., wildfires and soil carbon release). BBIO_SIB3 refers to a CO_2 emission dataset at 3-hourly intervals (2006–2010) derived from the Simple Biosphere Model version 3 (Parazoo et al., 2014). Figure 3f shows widespread positive emissions—up to about 40% of the maximum total emissions—except in South America and southern Africa, where tropical humid forests act as carbon sinks.

The second component, the residual annual terrestrial exchange (NET_TERR_EXCH), represents the net annual sum of biospheric CO_2 uptake and emissions. This dataset provides a single time slice for 1 January 2000 and was constructed as the TransCom-3 climatology (1991–2000) minus the GFEDv2 climatology (1997–2007) (Baker et al., 2006; van der Werf et al., 2006). In the TransCom framework, the residual annual biospheric flux includes gross primary productivity (GPP), respiration, and biomass burning; because biomass burning is accounted for separately in GEOS-Chem, the GFEDv2 climatology was subtracted from the TransCom climatology to estimate this component (Nassar et al., 2010). Figure 3g shows widespread terrestrial CO_2 uptake that is roughly 50% larger than the oceanic uptake.

In Figure 4a, total positive emissions in the Northern Hemisphere are driven mainly by fossil-fuel and aviation sources. Ship emissions are minor overall because they are largely offset by ocean uptake. Positive emissions in northern South America, northern Africa, and Australia are primarily from ecosystem sources. Total negative emissions are generally small but

https://doi.org/10.5194/egusphere-2026-4830
Preprint. Discussion started: 20 August 2026

widespread over mid- to high-latitude oceans; the largest negative emissions occur in southern South America and southern Africa, where terrestrial uptake is strongest.

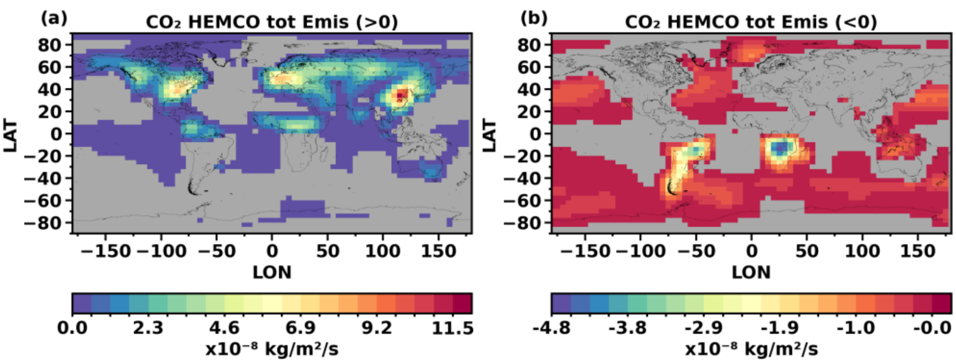

Figure 4: Total HEMCO CO2 emissions on 1 February 2019 shown as positive in (a) and negative in (b).

3.2. Other data sets

We used GEOS-FP (forward processing) meteorological analyses from the Global Modeling and Assimilation Office (GMAO) (GMAO Office Note No. 4), regridded for GEOS-Chem input at 5° longitude × 4° latitude. Hourly averages of temperature, wind, surface fluxes, moisture, cloud parameters, and precipitation were obtained for January and 1–8 February 2019. GMAO produces GEOS-FP using the Goddard Earth Observing System 5 (GEOS-5) model (USA symposium report, 2008), providing data in near-real time and via reanalysis. GEOS-FP's native horizontal resolution (0.3125° × 0.25°) is finer than that of the Modern-Era Retrospective Analysis for Research and Applications (MERRA) (0.66° × 0.5°).

This study also uses Level-2, geolocated, orbit-by-orbit XCO_2 (column-averaged CO_2 in ppm) from NASA's Orbiting Carbon Observatory-2 (OCO-2). Launched on 2 July 2014, OCO-2 is in a sun-synchronous orbit with a 13:30 equator crossing and provides near-global daily coverage. The accuracy and precision of OCO-2 XCO_2 have improved over time facilitated by advances in the Atmospheric Carbon Observations from Space (ACOS) retrieval algorithm (Wunch et al., 2017; O'Dell et al., 2018; Jacobs et al., 2024). For our analysis we used the 11.2r "lite" Level-2 product, which provides calibrated, bias-corrected orbit-by-orbit XCO_2. Aggregated to a 0.625°longitude×0.5° latitude grid, the data show absolute average biases ≤ 0.2 ppm and a global precision of ~1.0 ppm across all OCO-2 observation modes, with no statistically significant time dependence in the biases (Das et al., 2025). Findings in Crowell et al. (2019) suggest that: inverted fluxes from OCO-2 retrievals and from in-situ measurements show strong agreement in seasonal variability over Northern Hemisphere land regions for 2015–2016. Large uncertainties remain in the tropics—particularly Africa—where OCO-2–based inversions indicate possible outgassing. Ocean fluxes stay close to prior estimates but with substantial uncertainty. Agreement is strongest where both satellite and in-situ observations are sufficiently dense to constrain the inversion.

4. Model spin-up time

https://doi.org/10.5194/egusphere-2026-4830
Preprint. Discussion started: 20 August 2026

For carbon-flux inversions focusing on variability over days to months, long-lived gases like CO_2 can be treated as passive tracers. Oxidation products from CO, CH_4, isoprene, and monoterpenes are handled as CO_2 emission sources by including them in HEMCO with appropriate scaling factors. The downloaded restart file provides a reasonable background state. We then run the forward model with the current total emission field until it reaches steady state before performing the flux inversion.

To verify that a one-month spin-up is sufficient, we used two restart files to examine how long it took for the results to converge. The alternative restart file was created by combining OCO-2 data from 1 January and 1 July 2019 to capture both Northern and Southern polar coverages. The differences between this alternative restart file and the downloaded restart file were resampled along the OCO-2 orbital tracks, and the results were interpolated onto the GEOS-Chem grid to produce the bias field (GC minus OCO-2), shown in Figure 5c.

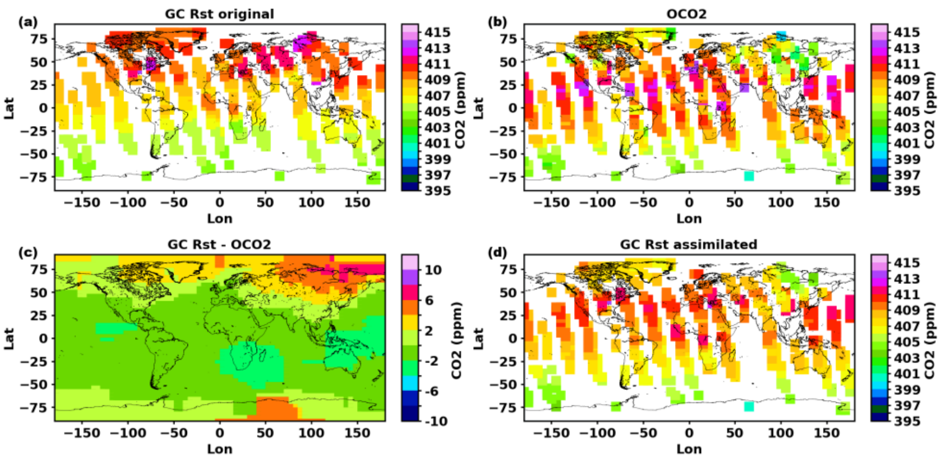

Figure 5: Bias correction of the GC restart file using OCO-2 data. (a) Initial GC restart XCO_2 field on 1 January 2019 (Rst1), sampled along OCO-2 tracks on 1 January and 1 July 2019 combined to cover both polar regions. (b) Co-located OCO-2 measurements. (c) Continuous bias field obtained by interpolating the differences between GC and OCO-2. (d) Final assimilated XCO2 field (Rst2) along OCO-2 tracks after bias correction.

Creating the alternative restart file also enabled a serendipitous assessment of bias patterns between the GC results and OCO-2 measurements. The bias patterns indicate that the high-value latitudinal bands in the GC restart file are shifted northward relative to OCO-2. Consequently, OCO-2 shows lower values in the northern polar region, compressing the high-concentration band toward the equator.

Next, we ran GEOS-Chem for one month using both restart files and compared the results. The daily differences between the two fields, in terms of global maximum (and minimum), decreased rapidly during the first week and then the rate of decrease slowed. Throughout January the magnitudes decrease from about 7 ppm (and -3.5 ppm) to roughly 1.2 ppm (and -1.5 ppm) (Figure 6a). The magnitudes on 31 January are comparable to OCO-2 XCO_2 uncertainty. By the end of the month the two XCO_2 fields had very similar spatial distributions, and their correlation coefficient became much higher (from 0.63 to 0.98 as

https://doi.org/10.5194/egusphere-2026-4830
Preprint. Discussion started: 20 August 2026

shown in Figure 6b). These results indicate that after one month the simulated XCO_2 driven by the total emission field has largely lost memory of its initial restart state. We then proceed to carry out the inversion over 1–8 February 2019.

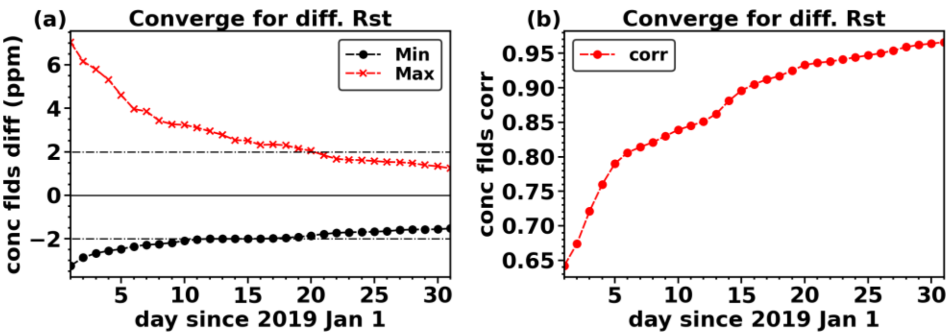

Figure 6: Comparison of GC-modeled XCO_2 over 1–31 January 2019 using initial conditions Rst1 and Rst2 (described in Figure 5). (a) Daily maximum (black) and minimum (red) differences between $XCO2_{Rst1}$ and $XCO2_{Rst2}$. (b) Correlation coefficients between the two daily-averaged XCO_2 fields over January 2019.

5. Inversion results

5.1. Under FullC condition

5.1.1. Convergence to T0 with different prior SF disturbance sets

Our first objective is to test how well the inversion works when pseudo-observations are generated from the original total emissions under FullC (see Figure 4). In this baseline case, the prior emission scaling factors (SFs) are perturbed around 1.0 (the default $\mathbf{x_a}$) and categorized as disturbed-pair, disturbed-three, sinusoidal-pair, and sinusoidal-three, spanning the state-vector space as described above. The sum of each set of prior SF perturbations is zero at each pixel. Figure 7 shows the ensemble mean of the inverted posterior SFs ($\hat{\mathbf{x}}$) for each set of prior SFs. Regions where the inversion result was trivial ($|\hat{\mathbf{x}} - 1.0| < 0.0015$) have been removed. All four panels in Figure 7 show posterior SF values consistently approaching 1.0 (mean deviation < 0.05), indicating near-perfect inversion when ensembles are used. In particular, random noise perturbations produce better convergence (i.e., closer to 1.0) than sinusoidal perturbations with variable phase. The sinusoidal case shows substantial continent-scale variability, suggesting slightly stronger nonlinear responses. In both the disturbed-pair/three and sinusoidal-pair/three cases, the three-ensemble means are closer to 1.0 than the two-ensemble means, implying that using more

https://doi.org/10.5194/egusphere-2026-4830
Preprint. Discussion started: 20 August 2026

ensemble members better mitigates nonlinear effects. This baseline case verifies that the analytic inversion converges nearly perfectly to the true solution for an 8-day inversion.

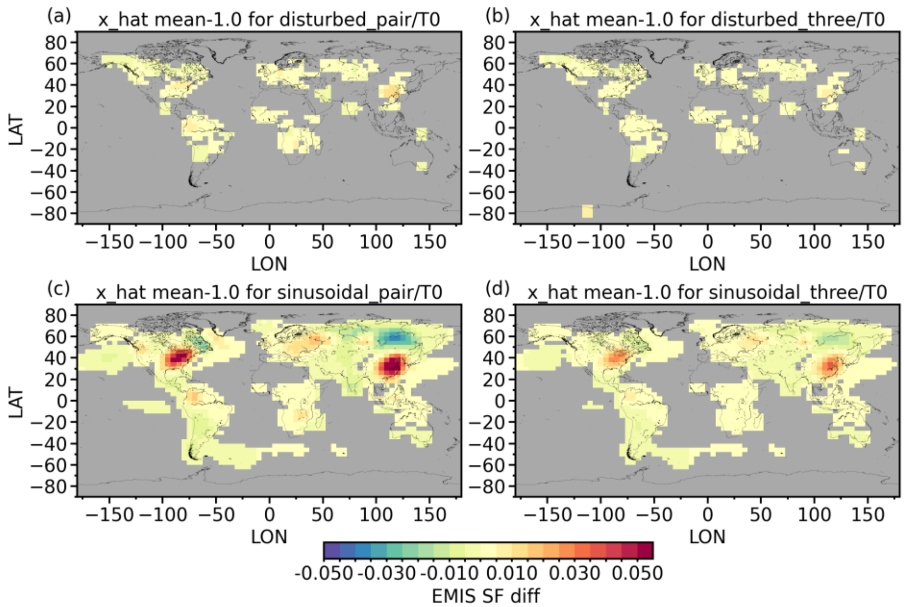

Figure 7: Convergence levels for the baseline case (using target zero, T0), as quantified by the deviation of the ensemble-mean $\hat{\mathbf{x}}$ from 1.0 for each of the four prior sets indicated in the panel titles. Values of $\hat{\mathbf{x}}$ near 1.0 (i.e., $|\hat{\mathbf{x}} - 1.0| < 0.0015$) are filtered out. A smaller threshold of 0.0015 (instead of 0.01) is used here to highlight the variability features, since convergence is near-perfect.

5.1.2. How T1, T2, and T3 are approached

For T1–T3, the ensemble-mean $\hat{\mathbf{x}}$ is not expected to converge exactly to the target SF; rather, the constrained solution lies between the prior and target SF fields. Figure 8b shows the inverted SF's maximum line near 25° longitude instead of 0°, where T1 peaks. Figures 8c and 8d are out of phase, as is the case for T2 versus T3. Overall, the maps in Figure 8 indicate that the inverted SFs capture the longitudinal variability of target SFs, but are strongly modulated by the model's sensitivity to emission changes; in low-sensitivity regions, corrections to the prior SF are virtually zero. We also note that the maxima and minima of $\hat{\mathbf{x}}$ can exceed 1.25 or drop below 0.75, indicating a substantial deviation from the target SFs.

While Figure 8 demonstrates that the mean $\hat{\mathbf{x}}$ across all prior sets converges well—though to varying degrees—for targets T1–T3, we next investigate how this performance differs by prior set; recalling that for T0, the level of convergence does change slightly by the type of prior. Figure 9 illustrates the pixelwise variability of $\hat{\mathbf{x}}$ among different prior sets for each target individually, expressed as $\hat{\mathbf{x}}_{\mathbf{Max}} - \hat{\mathbf{x}}_{\mathbf{Min}}$.. The results are remarkably consistent across targets in both magnitude and spatial distribution, highlighting the land regions where emissions are the largest. Two key points are summarized: (1) for a given target there is always a small difference (in terms of $\hat{\mathbf{x}}_{\mathbf{Max}} - \hat{\mathbf{x}}_{\mathbf{Min}}$) between prior-disturbance sets, and (2) the consistency of

https://doi.org/10.5194/egusphere-2026-4830
Preprint. Discussion started: 20 August 2026

260 these differences across targets implies that a given target cannot be approached more closely by choosing a different
261 prior-disturbance set, confirming that the inversion results are generally robust for a given target (or pseudo-observation set).

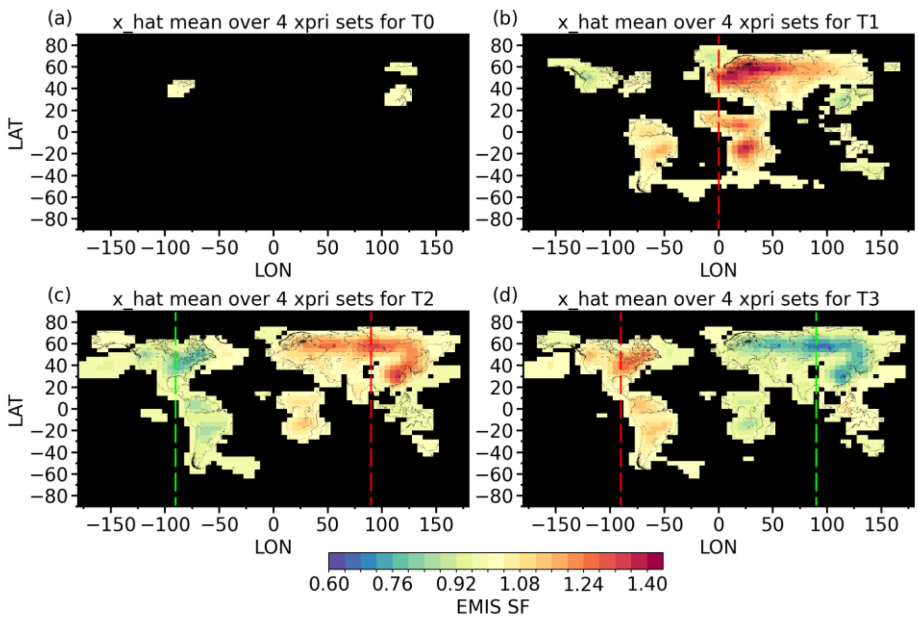

Figure 8: $\hat{x}$ averaged over all four prior sets for the individual targets T0 (a), T1 (b), T2 (c), and T3 (d), respectively. The red and blue long-dashed lines indicate the longitudes of the peaks and troughs of the target SFs shown in Figure 2. Values of $\hat{x}$ near 1.0 (i.e., $|\hat{x} - 1.0| < 0.01$) are filtered out.

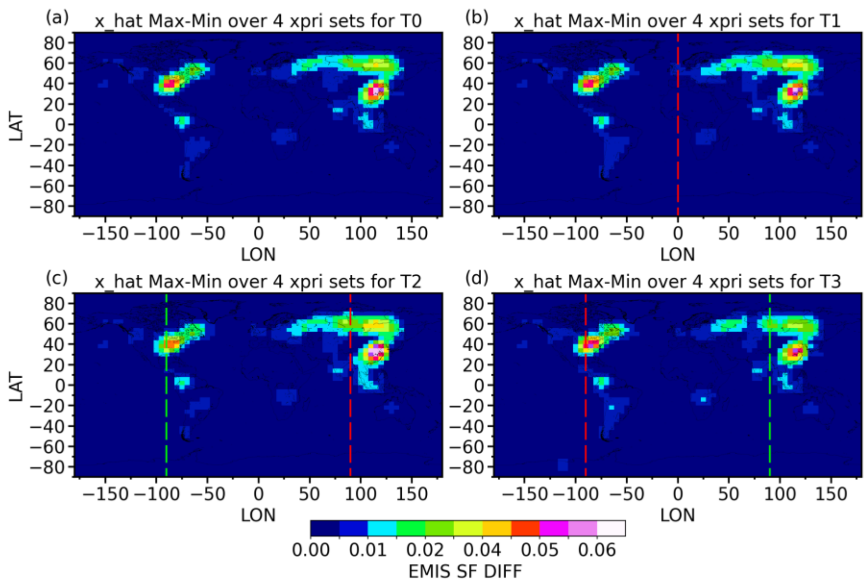

Figure 9: Max–Min values of $\hat{x}$ across the four prior sets for each target: T0 (a), T1 (b), T2 (c), and T3 (d). The red and blue long-dashed lines are the same as those shown in Figure 8.

262 **5.1.3. Posterior error matrix analysis**

https://doi.org/10.5194/egusphere-2026-4830
Preprint. Discussion started: 20 August 2026

The trace of the posterior error covariance matrix,

$$\hat{\mathbf{S}} = (\gamma\mathbf{K}^{\mathrm{T}}\mathbf{S}_{\mathrm{o}}^{-1}\mathbf{K} + \mathbf{S}_{\mathrm{a}}^{-1})^{-1} \quad (4),$$

serves as an estimate of the uncertainty reduction in $\hat{\mathbf{x}}$ given the observational error matrix **So**, the prior error matrix **Sa**, and the forward-model Jacobians. We set the prior emission uncertainty to 50%, the observational uncertainty to 4.0 ppmv, and the transport-induced uncertainty to 1.0 ppmv (the latter is incorporated into **So**). The observational uncertainty can be reduced when multiple observations fall within a single grid cell and when those observations are correlated (Chen et al., 2023). Two critical factors affect the spatial pattern of $\hat{\mathbf{x}}$ uncertainty: the Jacobians (forward-model sensitivity), and the spatiotemporal coverage (effective sample size). These factors highlight the roles of observations and forward model in reducing prior

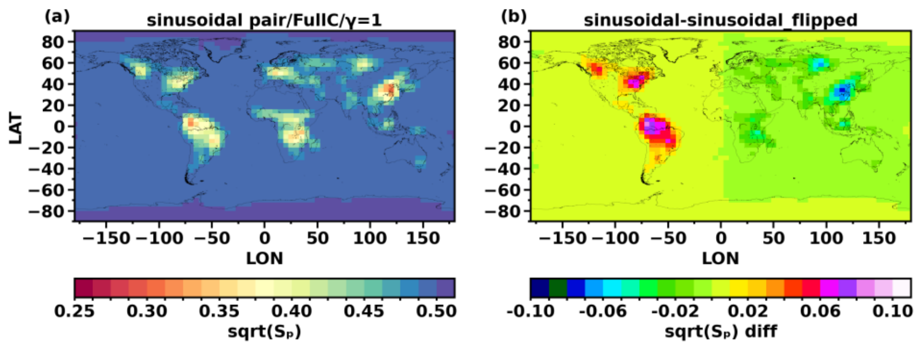

Figure 10: Posterior error related result from the inversion model standard output. (a) Mean posterior error field for runs using the sinusoidal-pair prior set with T0 as the target. (b) Error-difference field between the two runs associated with the sinusoidal-pair.

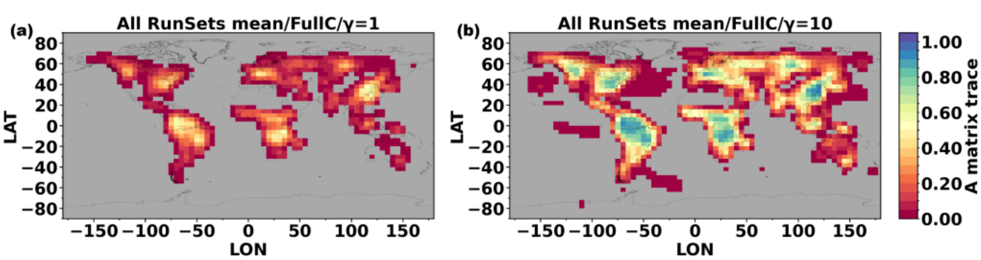

Figure 11. A-matrix trace values shown as 2D maps for γ=1 (a) and γ=10 (b), averaged over runs using all combinations of prior sets and targets.

emission uncertainty.

Figures 10a and 10b show the global distribution of mean uncertainty reduction and its variability across individual ensemble runs, using the sinusoidal-pair prior combined with target T0. Figure 10a indicates uncertainty reductions of roughly 10–20% from the initial 50% prior error. Figure 10b shows that higher emissions correspond to larger reductions, with a global maximum difference of about 8% between the pair. Regions with the strongest uncertainty reduction in Figure 10a coincide with areas of large variability in $\hat{\mathbf{x}}$. In addition, the uncertainty reduction values depend on γ: a large uncertainty reduction could easily arise from insufficient weighting of the prior during flux estimation (Basu et al., 2016). Viewed from another perspective, Figure 11 shows the trace of the A-matrix ($\partial\hat{\mathbf{x}}/\partial\mathbf{x_a}$) for γ = 1 and γ = 10. For γ = 10 (Figure 11b), much larger regions exhibit values near 1.0, reflecting an increased influence of the transport model, although very large γ eventually produces unrealistic fluctuations in $\hat{\mathbf{x}}$ (Hansen, 2000).

Finally, we propose a possible explanation for why error reduction remains consistently small over oceans compared with land. Although ocean emission variability is substantial (see Figure 3e), both magnitudes and their sensitivities are roughly an order of magnitude smaller than over land. This disparity limits the inversion algorithm's ability to adjust the emission SF and to reduce uncertainty in oceanic regions.

5.1.4. Individual runs

To evaluate how effectively individual ensemble members converge to the target SF, we next present maps of individual ensemble runs, comparing the initial difference and the posterior difference from the target. Figure 12 shows the maps for $\mathbf{x_a} - \mathbf{x_T}$. Figures 12a and 12b combine the sinusoidal-pair prior with T2 to test an in-phase and out-of-phase mismatch, since T2 is in phase with one member of the pair; this allows us to examine the inversion result when there is asymmetry between the two members with respect to the target. In Figure 12a, the prior and target SFs are in phase, with a difference of only 0.05 in amplitude. By contrast, Figure 12b shows a large difference (0.45 in amplitude) because the two are out of phase. Figures 12c and 12d show similar initial differences, but for the disturbed pair combined with T0. In this case, the fields are out of phase on small spatial scales, but their differences from the target SFs are balanced, preventing large-scale asymmetry.

Figure 13 shows analogous difference fields (to Figure 12) using the posterior SFs by replacing $\mathbf{x_a}$ with $\hat{\mathbf{x}}.\mathbf{x}_a$. In all four runs, the post-inversion differences are drawn substantially toward zero. A closer look shows a slight overshoot in Figure 13a (pale blue versus yellow); a slightly smaller γ might correct that overshoot. Figure 13b, which corrects Figure 12b, shows posterior differences ($\hat{\mathbf{x}}.\mathbf{x_a} - \mathbf{x_T}$) approaching zero in continental cores but deviating near coasts. Those coastal deviations correspond to decreases in $\partial\hat{\mathbf{x}}/\partial\mathbf{x_a}$ shown in Figure 11.

By examining individual runs, we see the ensemble mean can be either closer to or farther from the target SF than its individual members. For example, averaging Figures 13a and 13b yields slightly better convergence than Figure 13b alone, but still worse than Figure 13a, where the prior SF was already near the target. In contrast, averaging Figures 13c and 13d outperforms either individual run, producing an ensemble SF field that approaches 1.0 almost precisely. Inspecting individual ensemble members

https://doi.org/10.5194/egusphere-2026-4830
Preprint. Discussion started: 20 August 2026

reveals which members are close to—or far from—the target SF; a strong convergence of a member can indicate that this particular disturbed prior SF field best corresponds to the observations.

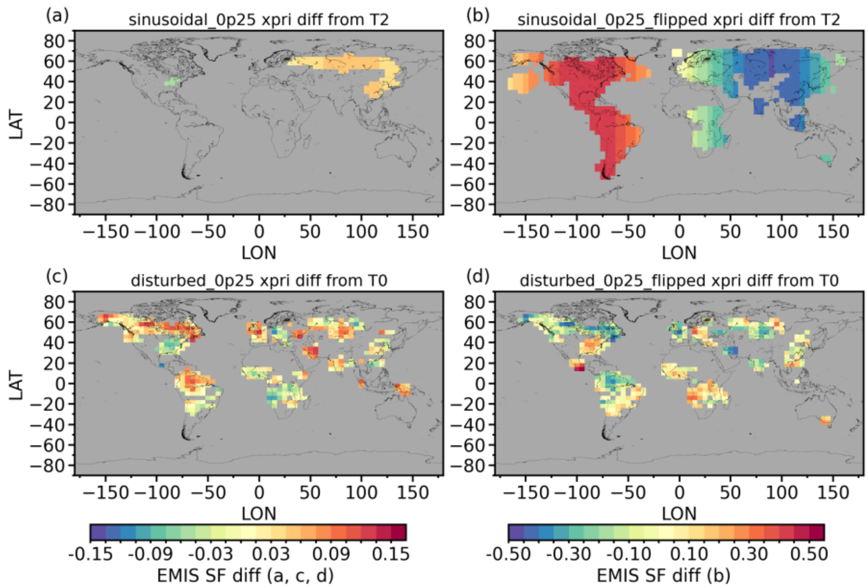

Figure 12: The individual ensemble members are shown by the difference between the prior SF and the target SF for two combinations of prior set and target: (a–b) the sinusoidal-pair run set combined with T2; (c–d) the disturbed-pair run set combined with T0.

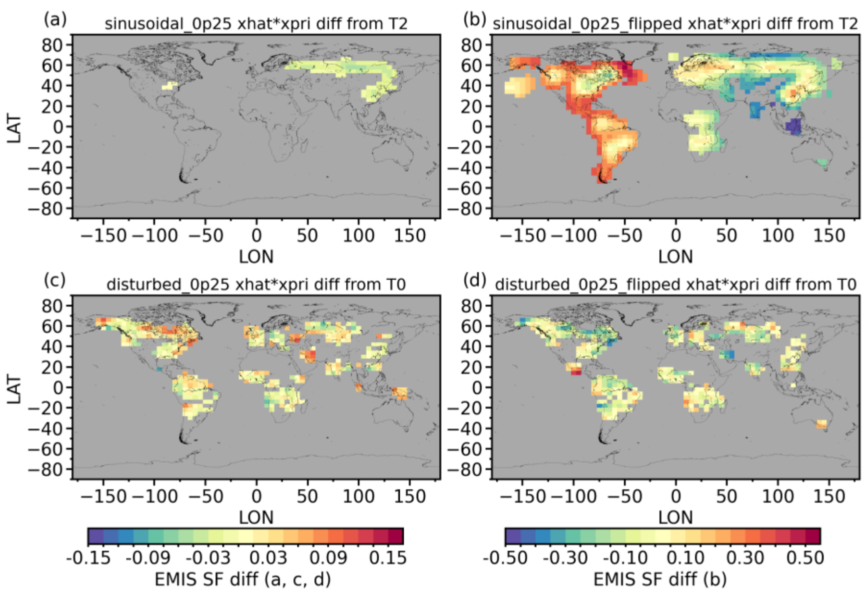

Figure 13: Similar to Figure 12, but with the prior SF replaced by the posterior SF to assess convergence toward the target. Good convergence is characterized by expanding regions where the values approach zero.

5.1.5. Histograms of prior and posterior differences from the target SF

https://doi.org/10.5194/egusphere-2026-4830
Preprint. Discussion started: 20 August 2026

Figures 14-17 summarize all individual runs and ensembles with histograms showing how closely the inverted SF matches the target SF. Each histogram plots the distribution of absolute differences $|\mathbf{x_a} - \mathbf{x_T}|$ (red) and $|\hat{\mathbf{x}}.\mathbf{x_a} - \mathbf{x_T}|$ (blue) across all pixels on a 4° latitude × 5° longitude grid. Only non-trivial inversions ($|\hat{\mathbf{x}} - 1| > 0.01$) were included. The black value in the legend marks half the maximum variability in $|\mathbf{x_a} - \mathbf{x_T}|$; the red and blue percentages give the fractions of $|\mathbf{x_a} - \mathbf{x_T}|$ and $|\hat{\mathbf{x}}.\mathbf{x_a} - \mathbf{x_T}|$ values below that threshold. The blue percentage is usually smaller than the red, and their difference quantifies the convergence level when $\mathbf{x_a}$ and $\mathbf{x_T}$ differ.

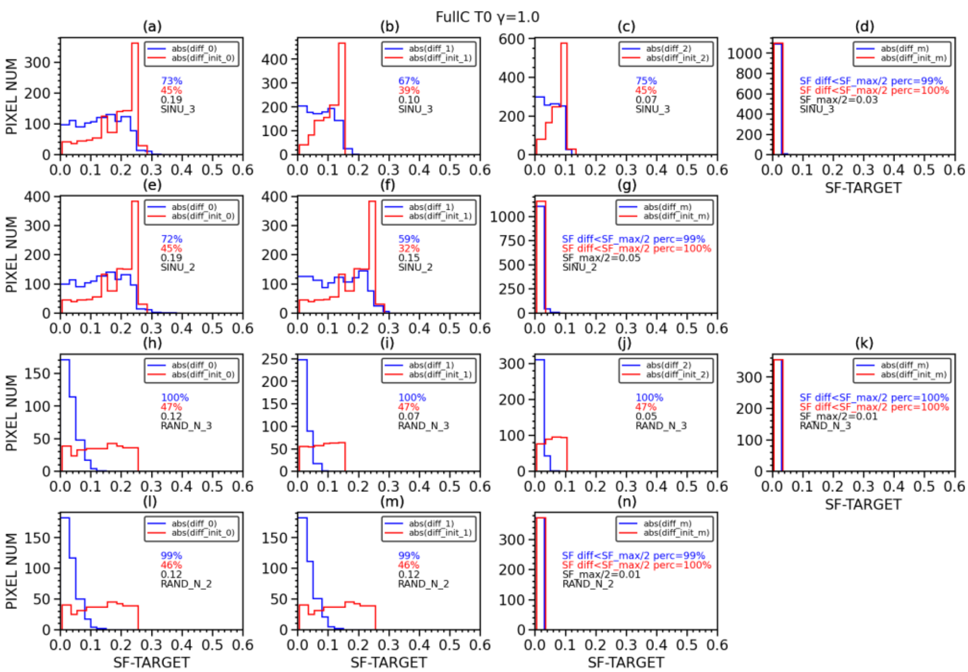

Figure 14: Histograms of absolute differences between the inverted and target SF (T0 for this figure) for individual runs and the ensemble mean. Rows correspond to different prior sets. Within each row, ensemble members are labeled diff_0, diff_1, and diff_2. Red and blue histograms show prior and posterior differences, respectively. Black numbers in the legends denote half of the peak frequency of the prior histogram, indicating its distribution spread. Detailed annotations are provided in the legends of the rightmost column.

When the target is T0, the histograms in Figure 14 indicate that ensemble means from all prior-SF sets converge to T0 nearly precisely, consistent with the findings in the $\hat{\mathbf{x}}$ ensemble maps (Figure 7). In the disturbed-pair and disturbed-three cases (Figures 14h–14j, 14l–14m), posterior differences transform from a roughly uniform distribution to a Gaussian-like distribution with minimal scatter. A similar transformation occurs for the sinusoidal-pair and sinusoidal-three cases (Figures 14a–14c, 14e–14f), but individual runs show poorer convergence because their initial differences are systematically larger, exhibiting continental-scale biases as evidenced by red histogram peaks that are significantly displaced from zero. The blue histogram for the ensemble-mean field in Figure 14g has a slight tail toward larger differences, indicating the sinusoidal-pair case converges slightly less well than the sinusoidal-three case.

https://doi.org/10.5194/egusphere-2026-4830
Preprint. Discussion started: 20 August 2026

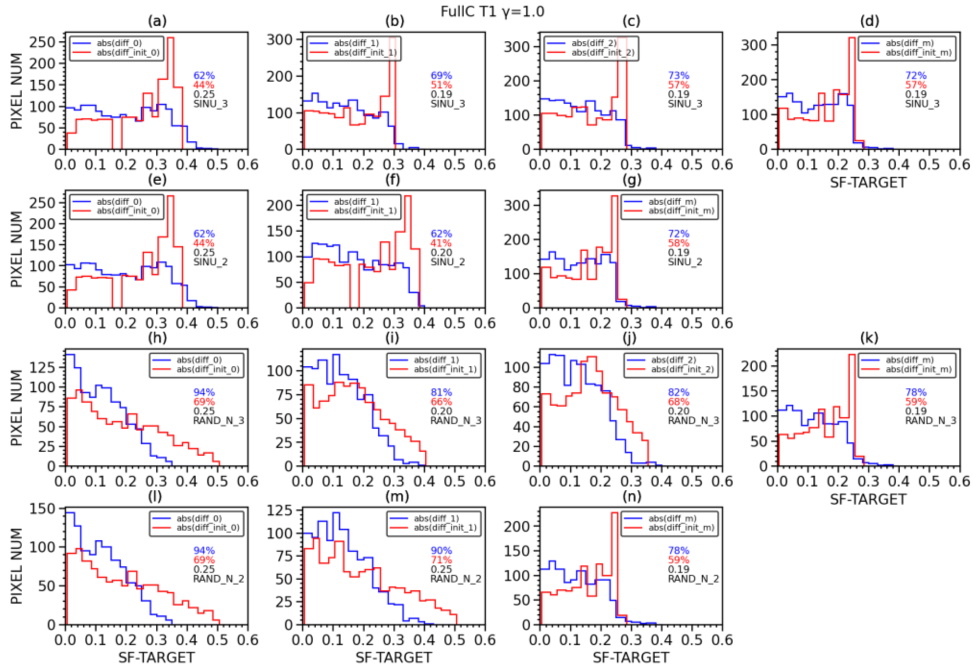

Figure 15: Same as Figure 14, except with T1 as the target.

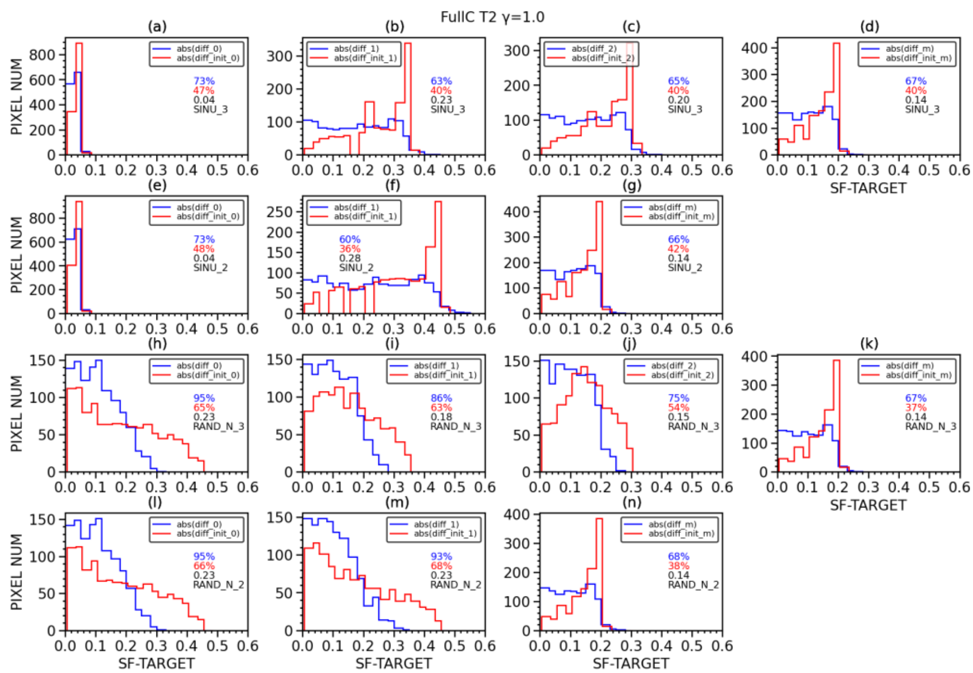

Figure 16: Same as Figure 14, except with T2 as the target.

https://doi.org/10.5194/egusphere-2026-4830
Preprint. Discussion started: 20 August 2026

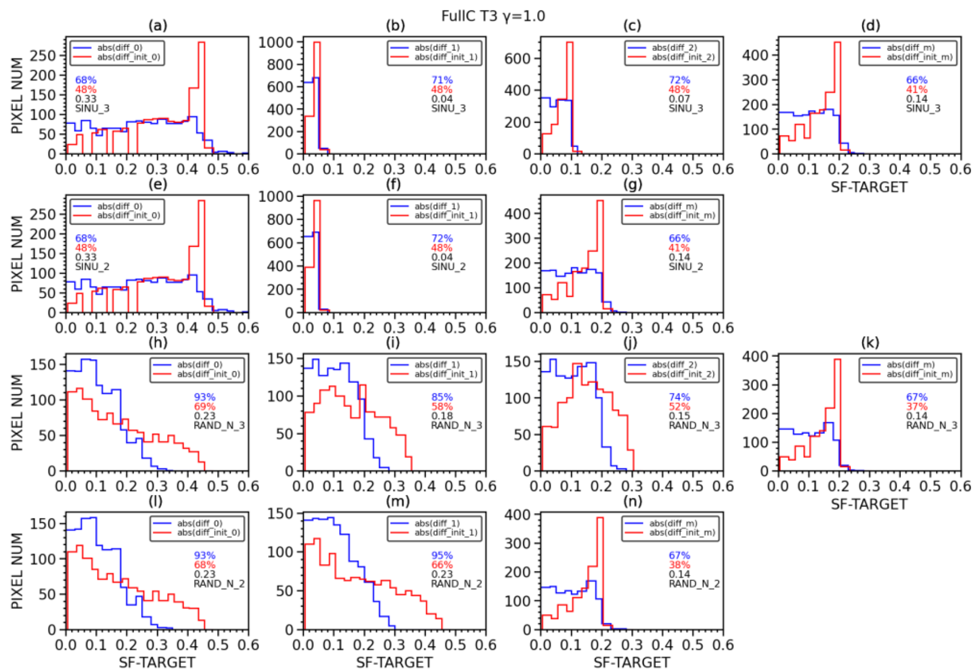

Figure 17: Same as Figure 14, except with T3 as the target.

Because T1 differs substantially from all prior sets—for instance, exhibiting a 90° phase shift relative to each of the sinusoidal-pair priors—the posterior differences ($|\hat{\mathbf{x}}.\mathbf{x}_a - \mathbf{x}_{T1}|$) reflect systematically poorer convergence, characterized by greater variability and broader peaks around zero. On a separate note, ensemble-mean distributions are remarkably similar across prior-SF types (Figures 15d, 15g, 15k, and 15n), indicating that prior-disturbance type does not change ensemble-mean convergence (as concurred in Figure 9). Examining the half-maximum widths (black values in legend), we note that the ensemble mean reduces variability relative to individual runs but does not bring the mean closer to T1; several individual runs (e.g., Figures 15h–15k) exhibit narrower peak regions around zero than the ensemble mean.

T2 (maximum in the East) and T3 are out of phase with each other, each having an amplitude of 0.2 and being in phase with one member of the sinusoidal-pair prior. For members aligned with T2 or T3 (Figures 16a and 17b), the posterior differences $|\hat{\mathbf{x}}.\mathbf{x}_a - \mathbf{x}_{T2/T3}|$ show further reduction toward zero with minimal scatter in the histograms. By contrast, the anti-phased prior member (relative to T2/T3) yields poorer convergence and much larger variability in $|\hat{\mathbf{x}}.\mathbf{x}_a - \mathbf{x}_{T2/T3}|$ (Figures 16f and 17e). This outcome is expected, and both histograms are qualitatively similar; however, convergence to T2 is better overall, showing a 24% improvement in the difference between the blue and red curves compared to 20% for T3. This disparity arises because the anti-phased member relative to T2 has a 25% deficit in the East, whereas the anti-phased member relative to T3 has a 25% surplus in the East with respect to the prior total emissions. Because the prior total emission field has its global maximum in China, a 25% increase yields a higher emission forcing, thereby generally worsening convergence.

https://doi.org/10.5194/egusphere-2026-4830
Preprint. Discussion started: 20 August 2026

5.2. Under oco2Trk condition

5.2.1. Comparison between oco2Trk and FullC for the pseudo-observations

Satellite measurements provide consistent, coherent spatiotemporal coverage, enabling meaningful global flux inversion. However, full spatiotemporal coverage at the given resolution is still the ideal scenario. Here, "full coverage" means the global 4° latitude × 5° longitude grid on an hourly basis. After resampling onto this grid, OCO-2 coverage (see Figure 5) accounts for less than 10% of the full coverage. For OCO-2-track inversions (oco2Trks) we use $\gamma = 10$; OCO-2-track-based inversions require a much larger γ for the posterior SF ($\hat{\mathbf{x}}$) to show notable variability. The γ=10 is close to optimal but may vary slightly with the target SF.

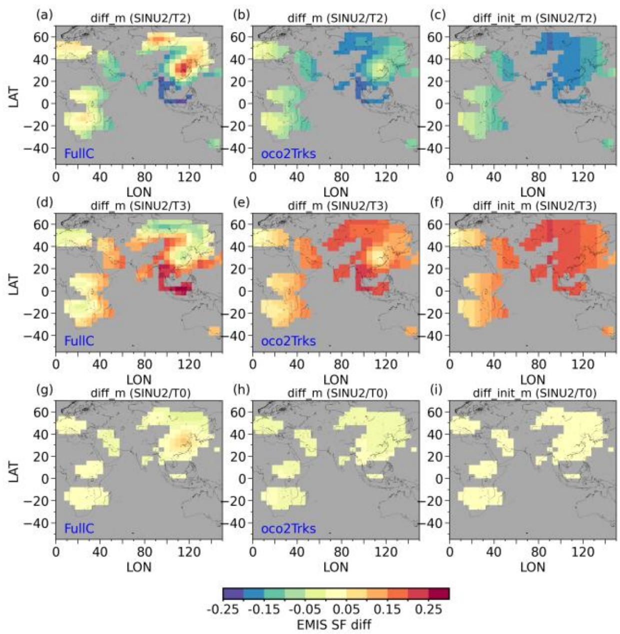

Figure 18: Comparison between the FullC and oco2Trks runs in terms of posterior (along with prior) SF deviations from the target; selected cases are shown, as indicated in subplot titles. Columns display FullC results (Column 1), oco2Trks results (Column 2), and prior differences (Column 3). Regularization parameters are set to γ = 1 for FullC and γ = 10 for oco2Trks. To highlight key features, only the Eastern Hemisphere is displayed.

Figures 18–19 show side-by-side difference maps (ensemble-mean posterior SF–target SF) for FullC and oco2Trks, respectively. Applying the criterion $|\hat{\mathbf{x}} - 1| > 0.01$ to oco2Trks reveals a much smaller area of non-trivial inversion than for FullC, despite oco2Trks using a larger γ. Adjusting γ can partly change this area by changing $\hat{\mathbf{x}}$ magnitudes, but the primary cause is the much poorer spatiotemporal coverage of oco2Trks. We do not observe any identifiable satellite footprints—such as those shown in Figure 5—in these maps. The spatial variability of $\hat{\mathbf{x}}$ is strongly correlated between FullC and oco2Trks. In the Eastern Hemisphere (around China), FullC shows an overshoot relative to zero, as shown in Figures 18a and 18d. In the Western Hemisphere, oco2Trks produce notably weaker deviations from the initial differences than FullC (Figures 19a, 19d,

https://doi.org/10.5194/egusphere-2026-4830
Preprint. Discussion started: 20 August 2026

and 19g versus 19b, 19e, and 19h), with FullC showing closer convergence toward zero. In summary, corrections are consistently larger in the East than the West under a globally uniform γ, likely because higher prior total emissions in China produce greater sensitivity in that region.

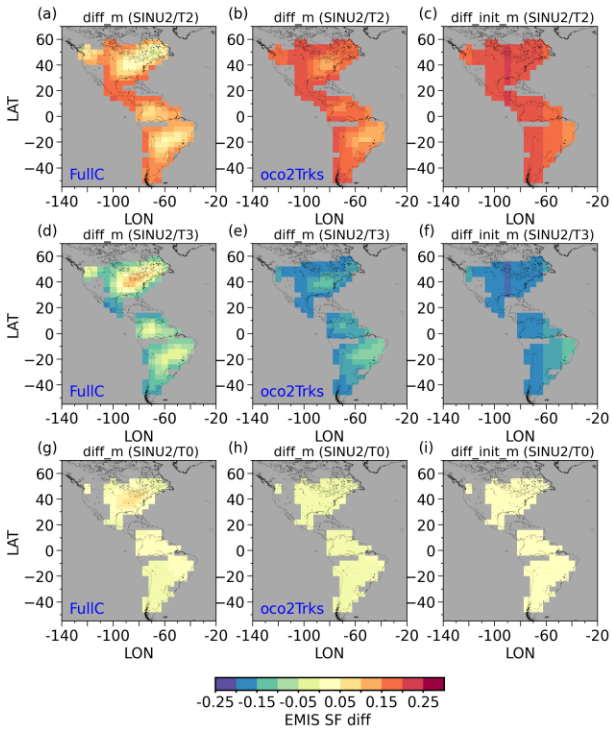

Figure 19: Same as Figure 18, but for the Western Hemisphere.

Figure 20 presents histograms (analogous to Figures 14–17) for OCO-2-track inversions (γ = 10) for T0. As in FullC, the ensemble-mean $\hat{\mathbf{x}}$ converges nearly exactly to 1.0, but individual-member performance depends on the prior SF. For disturbed-pair and disturbed-three priors the distributions are approximately Gaussian and centered on zero with minimal scatter, similar to FullC. By contrast, sinusoidal-pair and sinusoidal-three priors—which exhibit a strong global bias—show much poorer convergence for individual runs on oco2Trks: in Figures 20a–20c and 20e–20f the peaks shift toward but do not center on zero, indicating a smaller degree of adjustment of the posterior SFs compared with FullC. The same behavior occurs for T1–T3. Adjusting γ can improve convergence, but it is uncertain whether it will qualitatively change the histogram shapes.

https://doi.org/10.5194/egusphere-2026-4830
Preprint. Discussion started: 20 August 2026

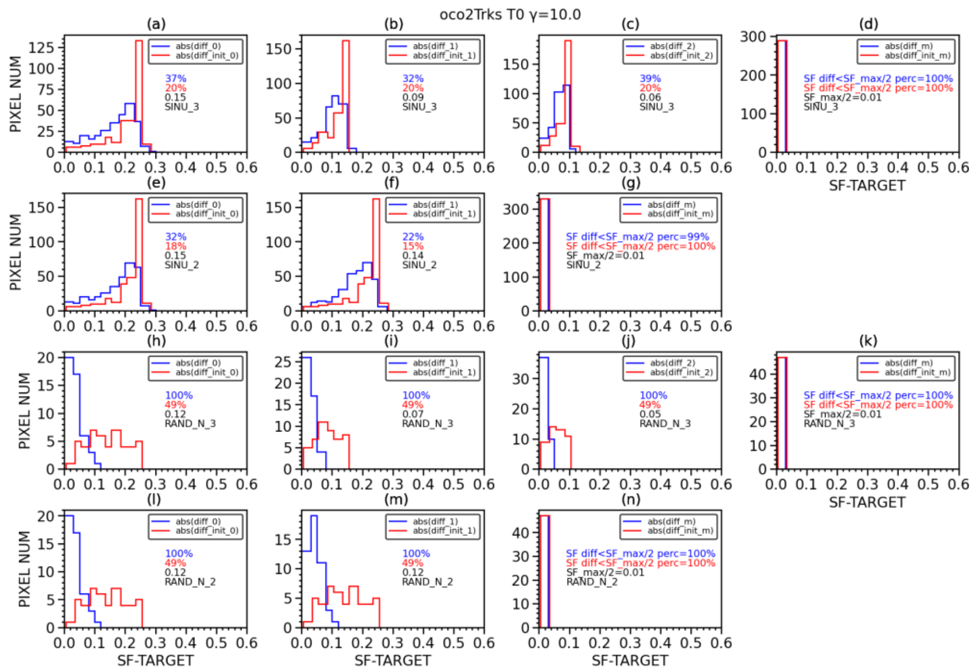

Figure 20: Histograms presented as in Figure 14, but using the inversion results for oco2Trks.

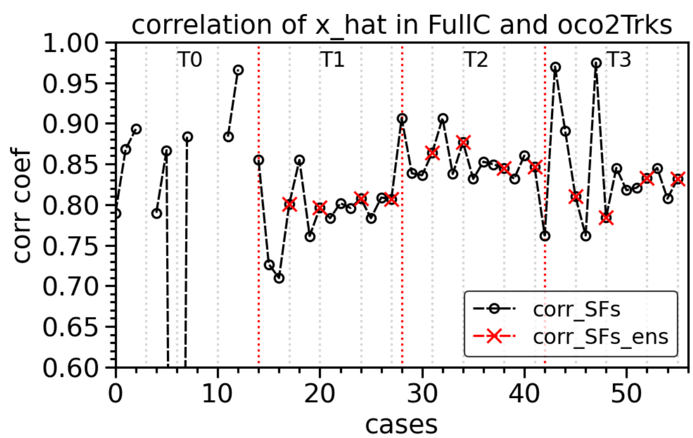

Figure 21: Line plot of spatial correlation coefficients between the FullC and oco2Trks posterior SF fields across all individual runs and their respective ensemble means. Vertical grey dotted lines separate the different prior sets in the following sequence: sinusoidal-three, sinusoidal-pair, disturbed-three, and disturbed-pair. Red crosses indicate the ensemble mean for each set; crosses are absent for certain sets because their ensemble-mean values are uniformly close to 1.0.

Figure 21 summarizes the comparison between FullC and oco2Trks across all prior–target SF combinations using their spatial correlation coefficients. Correlations are computed using sampling based on oco2Trks because their non-trivial inversion area is smaller. Overall correlations are high (≈0.85). Runs paired with T0 show the highest correlations; runs paired with T1 show the lowest, reflecting T1's largest bias relative to the priors. T2-related runs exhibit slightly better and more consistent

https://doi.org/10.5194/egusphere-2026-4830
Preprint. Discussion started: 20 August 2026

correlations than T3-related runs, reflecting the hemispheric asymmetry noted earlier. Overall, Figures 17–21 show that oco2Trks produce results qualitatively similar to FullC despite a substantially reduced area of non-trivial inversion due to poorer spatiotemporal coverage. Regions of non-trivial inverted SFs do not align with satellite footprints but instead occur where model sensitivity is higher, consistent with FullC.

5.2.2. Inversion result for OCO2 measurements

We next set the target to the OCO-2 observations (T_oco2) and run all prior-disturbance types with $\gamma = 10$. Figure 22 shows the resulting mean SF fields from all runs: Figure 22a is the ensemble mean $\hat{\mathbf{x}}$ and Figure 22b is the ensemble mean $\hat{\mathbf{x}}.\mathbf{x_a}$. The close agreement between the two panels confirms the inversion's robustness, since $\hat{\mathbf{x}}.\mathbf{x_a}$ typically amplifies the nonlinear features present in $\hat{\mathbf{x}}$.

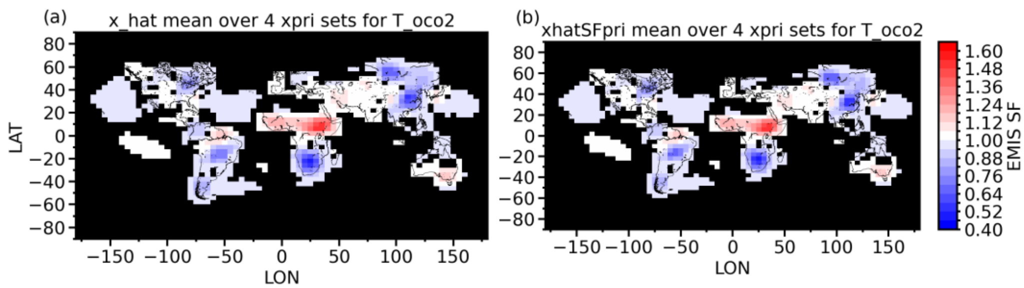

Figure 22: Inverted SF field using OCO-2 observations instead of the pseudo-observations corresponding to the target SFs shown in Figure 2. These runs also used $\gamma = 10$. (a) Mean $\hat{\mathbf{x}}$ across runs using all prior sets. (b) Each $\hat{\mathbf{x}}$ was first multiplied by its prior SF, and then the results were averaged.

Alongside Figure 22, we revisit Figures 4 and 5 to examine the global prior emission fields and OCO-2 observations, respectively. Figure 5 shows a low bias in OCO-2 measurements relative to GC concentrations at high latitudes during the inversion period. Although OCO-2 concentrations are generally higher between 50°S and 30°N, the high-latitude Eastern-Hemisphere low bias extends southward and affects regions such as China. Corresponding to this mid-to-high-latitude low bias, Figure 22 shows widespread reductions in SF ($\hat{\mathbf{x}} < 1$) in those regions. By contrast, posterior SFs over India and Europe are near or slightly above 1.0. Along the U.S. east coast, posterior SFs are below 1.0 but with a much smaller deficit than in China. Assuming these SF reductions in North America and China mirror the T2/T3 target experiments (Figures 18–19): with oco2Trks and $\gamma = 10$, posterior corrections toward T2/T3 are weaker for North America (Figures 19b, 19e) but substantially stronger around China (Figures 18b, 18e). This east–west asymmetry revealed in Figures 18–19 suggests that SF adjustment toward lower emissions in North America may be stronger than indicated in Figure 22.

Emissions in southern Africa and southern South America are negative in Figure 4, indicating surface uptake (downward concentration flux) in those areas. Figure 22 shows posterior SFs below 1.0 in both regions, suggesting actual uptake is smaller than indicated by the prior emissions. Overall, Figure 22 matches the bias pattern in Figure 5c, but these results should be interpreted with caution because the bias pattern in Figure 5c could also be caused by other factors, such as an imperfect

https://doi.org/10.5194/egusphere-2026-4830
Preprint. Discussion started: 20 August 2026

forward model or wind fields with substantial errors. Previous work (Wang et al., 2022) using Tansat CO_2 and the GEOS-Chem adjoint also found increased land sinks (less emissions) at mid–high latitudes and reduced sinks in the tropics relative to prior estimates.

5.3. The γ dependency

Stable solutions to the inversion problem through minimizing the cost function require a trade-off between two metrics: one pertains to the regularized solution, while the other describes the quality of the fit to the observational data, typically illustrated by an L-curve (Hansen, 1999). The dependence on the tuning parameter γ in carbon flux inversions has been discussed elsewhere (e.g., Qu et al., 2021; Lu et al., 2021; Chen et al., 2023). In this study, we used pseudo-observation fields derived from the target SFs, so we adopted a different fit metric rather than using posterior and prior concentrations.

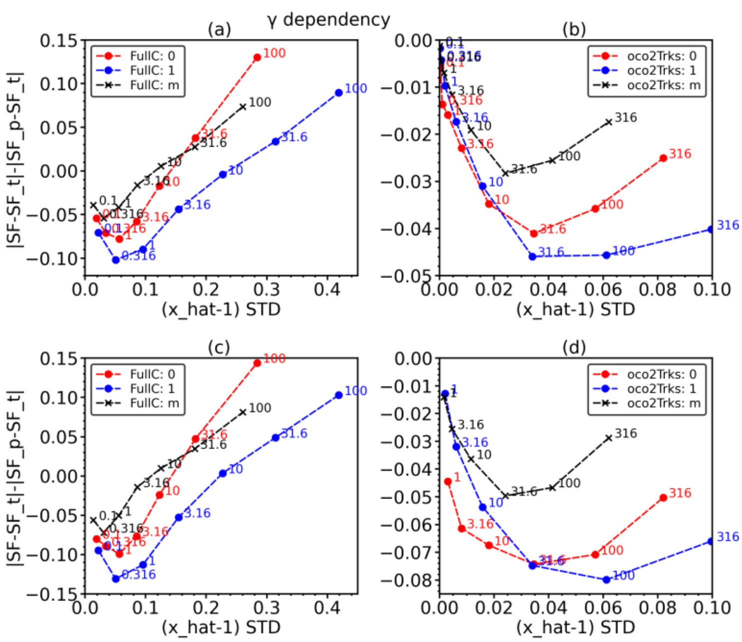

Figure 23: γ-dependency curves for the prior sinusoidal-pair set combined with T1, with γ values labeled next to each data point. The left and right panels show results for the FullC and oco2Trks runs, respectively. The x- and y-axes correspond to $\hat{\mathbf{x}}$ variability (in STD) and fit-quality indices (definitions in Section 5.3). Red, blue, and black curves show the fit-quality indices for the two individual runs and their ensemble mean, respectively.

We select a range of γ values, 10^{α}, where α takes the values -1, -0.5, 0, 0.5, 1, 1.5, and 2, corresponding to respective values 0.1, 0.316, 1, 3.16, 10, 31.6, and 100. Previously we used SF differences from the target as measures: $|\mathbf{x_a} - \mathbf{x_T}|$ is the initial (prior) deviation and $|\hat{\mathbf{x}}.\mathbf{x_a} - \mathbf{x_T}|$ is the posterior deviation. The operator $|\cdot|$ denotes the global mean of pixel-wise absolute differences. We define fit quality as $|\hat{\mathbf{x}}.\mathbf{x_a} - \mathbf{x_T}| - |\mathbf{x_a} - \mathbf{x_T}|$. A more negative value of this metric means two things: (1) the posterior SF moves closer to the target overall, and (2) global variability in the posterior SF is not dominated by large local fluctuations that arise when inversion becomes unstable. Unlike a standard L-curve metric, this measure captures the

https://doi.org/10.5194/egusphere-2026-4830
Preprint. Discussion started: 20 August 2026

degradation in fit as γ increases indefinitely; in this case, large point-to-point variability or checkerboard patterns would appear in $\hat{\mathbf{x}}$. The metric's dependence on γ has a turning point, which makes the optimal γ easier to identify.

Figure 23 shows the γ-dependency curves for the case using T1 combined with the sinusoidal-pair prior. T1 was chosen because the associated convergence level in $\hat{\mathbf{x}}$ is generally poorer, and we wanted a challenging case to construct the γ-dependence curve. We used the standard deviation of $\hat{\mathbf{x}}$ as the metric for the regularized solution. Two sampling thresholds for $|\hat{\mathbf{x}} - 1|$ (>0.05 and 0.1) produced the slightly different γ-dependency curves shown in the upper and lower panels, respectively. The left and right panels show FullC and oco2Trks, respectively. Within each panel the three curves are roughly consistent. For FullC the minimum occurs at $\gamma = 0.316$ or 1.0. Although the two thresholds (0.05 and 0.1) shift the curves vertically, they do not change the γ at which the minimum occurs. Because the oco2Trks coverage is less than one-tenth of FullC, the optimal γ is much larger (≈31.6–100) in the right panel. For FullC, $\gamma > 10$ produces rapidly increasing noise that worsens convergence toward the target. The variability around the turning point for oco2Trks is asymmetric and decays more slowly with increasing γ, which may be due to poor spatiotemporal coverage; as shown above, we found that much larger γ is required to produce notable variability in $\hat{\mathbf{x}}$. The exact turning-point γ can vary slightly with the chosen target and would require more experiments to determine precisely.

6. Discussion and conclusions

In this study, we developed an Adapted Analytic CO_2 Flux Inversion Model (AACO_2FIM) based on the Integrated Methane Inversion (IMI) system. Specifically, we modified the original CO_2 code in GEOS-Core to add emission-perturbation capability for calculating Jacobians, and scaling-factor (SF) capability for emissions. We also incorporated two spatiotemporal coverage schemes into the inversion package. Our overarching goal is to expand the existing suite of top-down inversion frameworks, enabling future multi-model and cross-model validations. Ultimately, such advancement aims to enhance the accuracy of top-down estimation techniques, making them a more practical and reliable tool for societal decision-making. We evaluated the performance of the AACO_2FIM framework specifically focusing on its inversion model, while assessing how the regulated solution is affected by spatiotemporal coverage. The system ingested the best available CO_2 inventories, forward-model pseudo-observations, and OCO-2 satellite observations as primary inputs.

Carbon dioxide emission inventories were aggregated onto a user-defined grid using GEOS-Chem HEMCO diagnostics, as summarized below: Fossil fuel emissions from land in the Northern Hemisphere are the largest contributors, typically accounting for over 80% of total emissions at main-emission centers in the Northern Hemisphere; for example, Eastern China can reach 10×10^{-8} kg/m²/s. Ocean exchange exhibits more diffuse patterns and vary with latitude: near the equator emissions are slightly positive at 0.2×10^{-8} kg/m²/s, while mid-to-high latitudes typically show negative values, ranging from -0.5 to -1.0×10^{-8} kg/m²/s, indicating net absorption. The Balanced Biosphere and Net Terrestrial Exchange include wildfires, soil dissolution, plant photosynthesis, and respiration. Over Northern Hemisphere land, these processes account for at least 30%

https://doi.org/10.5194/egusphere-2026-4830
Preprint. Discussion started: 20 August 2026

of positive emissions; in the Southern Hemisphere (notably southern South America and southern Africa) they exhibit net negative values, offsetting the emission sources.

Assessing uncertainty in top-down carbon flux inversion is essential to validate its reliability. Top-down methods estimate regulated emission scaling factors (SFs) via numerical modeling, reducing subjectivity, but uncertainties from the forward model, inversion model, meteorological data, prior emissions, and observations must be contained (Wolden et al., 2022). Using various forward transport models, previous studies show model-dependent but generally moderate errors. For instance, Pickett-Heaps et al. (2011) found biases and RMS differences across transport models typically within ~1.0 ppm, providing basic confidence in using different transport models. Regarding inversion algorithms, Bousserez et al. (2015) reported similar error-reduction patterns between Monte Carlo and variational methods, despite their different convergence rates. Focusing on the effect of observations, Liu et al. (2016) demonstrated that inversion results become less dependent on inversion methods as the coverage of observations increases. Lagrangian dispersion models (e.g., WRF-HYSPLIT) are another suite of transport frameworks that are desirable for regional studies because of lower computational cost and simplicity. For example, the results of WRF-HYSPLIT compare reasonably well with those of WRF-Chem in sub-daily CO_2 variability despite differences in vertical structure (Karion et al., 2019). These cross-model comparisons demonstrate basic consistency, even though different models may share similar biases. Such a consistency supports pursuing specific models for operational purposes. To do so, we must quantify inversion uncertainty in greater detail. In this paper, we first adapt the IMI to facilitate CO_2 inversion and then assess the resulting performance under several combinations of prior and target emission settings.

The inversion algorithm is typically developed for specific satellite spatiotemporal coverage; here we utilized OCO-2 orbital tracks (oco2trks). We also employed a global grid (4° latitude × 5° longitude) as an ideal coverage (FullC) to test variability of the inversion results to spatiotemporal coverage. Meanwhile, forward model sensitivities (Jacobians) strongly influence inversion results: because ocean emissions are much lower and spatially smoother, the Jacobians show minimal responses to percentage changes in prior emissions, so the inversion cannot effectively adjust prior emissions over oceans. Even improved or complete spatiotemporal coverage does not change this limitation.

To evaluate the performance of AACO_2FIM, we used predetermined target SFs to generate several spatiotemporal distributions of pseudo-observations. We then examined how the regulated solution (the inverted SF) responds and converges toward these targets. The target SFs were longitudinal wave-1 with amplitudes $\leq$0.25 and varying phases. We also created multiple prior disturbance sets (each with pixelwise ensemble mean of zero), consisting of either random noise across state-vector elements or the aforementioned longitudinal wave-1 pattern.

In the first experiment, the observation proxy was driven by prior emissions with no scaling applied (SF $\equiv$1.0). In this case, the ensemble mean of the inverted SFs lies within 1.0 ± 0.05—with the largest discrepancies occurring when the sinusoidal prior disturbance is applied—indicating extremely close convergence toward 1.0 overall. This experiment validates the

https://doi.org/10.5194/egusphere-2026-4830
Preprint. Discussion started: 20 August 2026

inversion model, yielding similar results to previous work, such as Niwa et al. (2022), who utilized an iterative variational method.

When the target SF field is biased relative to the prior SF, the inverted (regulated) SF generally falls between the prior and target, though the degree of convergence toward the target varies widely across the domain. The inverted SF field obtained with the optimal (globally consistent) γ shows the best alignment with the target and reproduces its longitudinal variability (as we used a wave-1 longitudinal variability pattern). A closer examination shows that where the forward-model sensitivity to emission changes is significant (the main emission centers), the posterior SFs approach the target effectively. However, when the prior and target bias is large (for example, caused by a 90° phase shift), poorly contained variability can occur in those centers, such as over-shooting. By contrast, inversion is ineffective ($\hat{\mathbf{x}} \approx 1.0$) in regions with low forward-model sensitivity, where the prior emissions are small or lack spatial variability (for example, over oceans). For a given inversion run, a pair of histograms showing prior-to-target and posterior-to-target SF differences (over all pixels) can be used to quantify convergence by comparing the percentages of values below a common threshold toward zero.

For the same pseudo-observational target SFs, inversions on OCO-2 tracks require a substantially larger optimal γ to produce a noticeable correction from the prior SF, but the area where the inversion produces nontrivial changes shrinks markedly because of the limited spatiotemporal coverage. Nevertheless, the inverted SFs from both coverage types remain strongly correlated, indicating that spatiotemporal coverage differences do not change the overall global variability of the inverted SF field.

Finally, original OCO-2 XCO_2 data from 1-8 February 2019 were used as the observations, and the global bias of these data from the GC-modeled concentrations was also calculated. The bias and the inverted SFs show overall good correspondence, indicating localized responses to emission deficits or surpluses on continental scales within the 8–day period. The inverted SFs indicate that mid- to high-latitude regions—particularly China—should exhibit lower emissions than the prior estimates, while lower-latitude regions, including parts of South America and Africa, are expected to have higher emissions or lower uptakes.

Concurrently, we introduced and computed a fit quality index—defined specifically for this study—is computed using the target SFs rather than forward-model or observational concentrations. With the regulatory parameter γ set to 0.1, 0.316, 1, 3.16, 10, 31.6, and 100, we find γ between 0.316 and 1.0 is optimal for the FullC cases. For poorer spatiotemporal coverage (e.g., oco2Trks), a significantly larger γ is required to reach the optimal fit quality.

Code and data availability

IMI and GEOS-Chem code packages can be downloaded from https://github.com/geoschem/integrated_methane_inversion . The webpage may change periodically. OCO2 level-2 data can be downloaded from https://disc.gsfc.nasa.gov/datasets?keywords=oco2 . The carbon dioxide (CO_2) emission inventories and Geos-FP data are automatically downloaded from Amazon Web Services (AWS) while running the IMI.

https://doi.org/10.5194/egusphere-2026-4830
Preprint. Discussion started: 20 August 2026

Author contributions

Pingping Rong conceived the research framework, executed the simulations, analyzed the results, prepared the figures, and drafted the manuscript. Hui Su provided administrative oversight, contributed to the conceptual design, guided the research direction, and critically reviewed the manuscript.

Competing interests

The authors declare no competing interests.

Financial support

This work was conducted at the HKUST JC STEM Lab of Convection and Precipitation, which is supported by the Hong Kong Jockey Club Charities Trust (FA123), the Innovation and Technology Commission project ITS/003/24SC (P0491) and the State Key Laboratory scheme under the Innovation and Technology Commission (ITC-SKLCRCC26EG01).

Acknowledgements

We thank the Information Technology Services Office (ITSO) at the Hong Kong University of Science and Technology (HKUST) for implementing and maintaining the fourth-generation high-performance computing cluster (HPC4), on which the simulations for this study were executed. We also thank the IMI Team at Harvard University for developing, maintaining, and open-sourcing the code package used in this study. We acknowledge the NASA Goddard Earth Sciences Data and Information Services Center (GES DISC) for making the OCO-2 data publicly available, and Amazon Web Services for facilitating access to some of the data used in this study. Additionally, we used the AI mode of several platforms to check the grammar and clarity of our writing. Finally, we are grateful to Prof. Lu Shen (Peking University) for insightful discussions during the early stages of this study, and to Prof. Zichong Chen (HKUST Guangzhou) for constructive feedback at the Net Zero Carbon Transition Workshop (28-29 October 2025, HKUST Hong Kong).

References

Baker, D. F., Law, R. M., Gurney, K. R., Rayner, P., Peylin, P., Denning, A. S., Bousquet, L. Bruhwiler, P. , Chen, Y.-H., Ciais, P., Fung, I. Y., Heimann, M., John, J., Maki, T., Maksyutov, S., Masarie, K., Prather, M., Pak, B., Taguchi, S., and Zhu, Z.: TransCom 3 inversion intercomparison: Impact of transport model errors on the interannual variability of regional CO_2 fluxes, 1988-2003, Global Biogeochem. Cy., 20, GB1002, doi:10.1029/2004GB002439, 2006.

Basu, S., Miller, J. B., and Lehman, S.: Separation of biospheric and fossil fuel fluxes of CO_2 by atmospheric inversion of CO_2 and $^{14}CO_2$ measurements: Observation System Simulations, Atmos. Chem. Phys., 16, 5665–5683, https://doi.org/10.5194/acp-16-5665-2016, 2016.

https://doi.org/10.5194/egusphere-2026-4830
Preprint. Discussion started: 20 August 2026

Bousserez, N., Henze, D. K., Perkins, A., Bowman, K. W., Lee, M., Liu, J., Deng, F. and Jones, D.B.A.: Improved analysis-error covariance matrix for high-dimensional variational inversions: application to source estimation using a 3D atmospheric transport model, Q.J.R. Meteorol. Soc., 141: 1906-1921. https://doi.org/10.1002/qj.2495, 2015.

Ciais, P., Rayner, P., Chevallier, F., Bousquet, P., Logan, M., Peylin, P., and Ramonet , M.: Atmospheric inversions for estimating CO_2 fluxes: methods and perspectives, Climatic Change, 103, 69–92 (2010). https://doi.org/10.1007/s10584-010-9909-3

Chen, Z., Jacob, D. J., Gautam, R., Omara, M., Stavins, R. N., Stowe, R. C., Nesser, H., Sulprizio, M. P., Lorente, A., Varon, D. J., Lu, X., Shen, L., Qu, Z., Pendergrass, D. C., and Hancock, S.: Satellite quantification of methane emissions and oil–gas methane intensities from individual countries in the Middle East and North Africa: implications for climate action, Atmos. Chem. Phys., 23, 5945–5967, https://doi.org/10.5194/acp-23-5945-2023, 2023.

Crisp, D., Dolman, H., Tanhua, T., McKinley, G. A., Hauck, J., Bastos, A., Sitch, S., Eggleston, S., and Aich, V.: How well do we understand the land-ocean-atmosphere carbon cycle? Reviews of Geophysics, *60*, e2021RG000736. https://doi.org/10.1029/2021RG000736, 2022.

Crowell, S., Baker, D., Schuh, A., Basu, S., Jacobson, A. R., Chevallier, F., Liu, J., Deng, F., Feng, L., McKain, K., Chatterjee, A., Miller, J. B., Stephens, B. B., Eldering, A., Crisp, D., Schimel, D., Nassar, R., O'Dell, C. W., Oda, T., Sweeney, C., Palmer, P. I., and Jones, D. B. A.: The 2015–2016 carbon cycle as seen from OCO-2 and the global in situ network, Atmos. Chem. Phys., 19, 9797–9831, https://doi.org/10.5194/acp-19-9797-2019, 2019.

Das, S., Kiel, M., Laughner, J., Osterman, G., O'Dell, C. W., Taylor, T. E., Fisher, B., Chevallier, F., Deutscher, N. M., Dubey, M. K., Feist, D. G., Garcia, O., Griffith, D. W. T., Hase, F., Iraci, L. T., Kivi, R., Morino, I., Notholt, J., Ohyama, H., Pollard, D., Roche, S., Roehl, C. M., Rousogenous, C., Sha, M. K., Shiomi, K., Strong, K., Sussmann, R., Té, Y., Toon, G., Vrekoussis, M., Wang, P. C., Warneke, T., Wennberg, P., Chatterjee, A., Payne, V. H., and Wunch, D.: Comparisons of the v11.1 Orbiting Carbon Observatory-2 (OCO-2) XCO_2 measurements with GGG2020 TCCON, Earth and Space Science, 12, e2024EA003935. https://doi.org/10.1029/2024EA003935, 2025.

Feng, L., Smith, S. J., Braun, C., Crippa, M., Gidden, M. J., Hoesly, R., Klimont, Z., van Marle, M., van den Berg, M., and van der Werf, G. R.: The generation of gridded emissions data for CMIP6, Geosci. Model Dev., 13, 461–482, https://doi.org/10.5194/gmd-13-461-2020, 2020.

GMAO Office Note No. 4 (Version 2.0), File Specification for GEOS FP (Forward Processing), 02/26/2026.

Hansen, P. C.: The L-curve and its use in the numerical treatment of inverse problems, Computatinal Inverse Problems in Electrocardiology, pp. 119-142, WIT Press, 2000.

https://doi.org/10.5194/egusphere-2026-4830
Preprint. Discussion started: 20 August 2026

Hantson, S., Knorr,W., Schurgers, G., Pugh, T. A. M., and Arneth, A., Global isoprene and monoterpene emissions under changing climate, vegetation, CO_2 and land use, Atmospheric Environment, 155, 35-45, https://doi.org/10.1016/j.atmosenv.2017.02.010., 2017.

Hoesly, R. M., Smith, S. J., Feng, L., Klimont, Z., Janssens-Maenhout, G., Pitkanen, T., Seibert, J. J., Vu, L., Andres, R. J., Bolt, R. M., Bond, T. C., Dawidowski, L., Kholod, N., Kurokawa, J.-I., Li, M., Liu, L., Lu, Z., Moura, M. C. P., O'Rourke, P. R., and Zhang, Q.: Historical (1750–2014) anthropogenic emissions of reactive gases and aerosols from the Community Emissions Data System (CEDS), Geosci. Model Dev., 11, 369–408, https://doi.org/10.5194/gmd-11-369-2018, 2018.

Hu, K., Feng, X., Zhang, Q., Shao, P., Liu, Z., Xu, Y., Wang, S., Wang, Y., Wang, H., Di, L., and Xia., M.: Review of Satellite Remote Sensing of Carbon Dioxide Inversion and Assimilation. Remote Sens. 2024, 16, 3394. https://doi.org/10.3390/rs16183394, 2024

Jacob, D. J., Turner, A. J., Maasakkers, J. D., Sheng, J., Sun, K., Liu, X., Chance, K., Aben, I., McKeever, J., and Frankenberg, C.: Satellite observations of atmospheric methane and their value for quantifying methane emissions, Atmos. Chem. Phys., 16, 14371–14396, https://doi.org/10.5194/acp-16-14371-2016, 2016.

Jacobs, N., O'Dell, C. W., Taylor, T. E., Logan, T. L., Byrne, B., Kiel, M., Kivi, R., Heikkinen, P., Merrelli, A., Payne, V. H., and Chatterjee, A.: The importance of digital elevation model accuracy in X_{CO2} retrievals: improving the Orbiting Carbon Observatory 2 Atmospheric Carbon Observations from Space version 11 retrieval product, Atmos. Meas. Tech., 17, 1375–1401, https://doi.org/10.5194/amt-17-1375-2024, 2024.

Karion, A., Lauvaux, T., Lopez Coto, I., Sweeney, C., Mueller, K., Gourdji, S., Angevine, W., Barkley, Z., Deng, A., Andrews, A., Stein, A., and Whetstone, J.: Intercomparison of atmospheric trace gas dispersion models: Barnett Shale case study, Atmos. Chem. Phys., 19, 2561–2576, https://doi.org/10.5194/acp-19-2561-2019, 2019.

Kim, B. Y., Fleming, G. G., Lee, J. J., Waitz, I., A., Clarke, J.-P., Balasubramanian, S., Malwitz, A., Klima, K., Locke, M., Holsclaw, C. A., Maurice, L. Q., and Gupta, M. L.: System for assessing Aviation's Global Emissions (SAGE), Part 1: Model description and inventory results, Transportation Research Part D: Transport and Environment, 12, 5, 2007, pp 325-346, https://doi.org/10.1016/j.trd.2007.03.007, 2007.

Kondo, M., K. Ichii, H. Takagi, and M. Sasakawa: Comparison of the data-driven top-down and bottom-up global terrestrial CO_2 exchanges: GOSAT CO2 inversion and empirical eddy flux upscaling, J. Geophys. Res. Biogeosci., 120, 1226–1245, doi:10.1002/2014JG002866, 2015.

Kondo M, Patra P. K., Sitch S., Friedlingstein, P., Poulter, B., Chevallier, F., Ciais, P., Canadell, J. G., Bastos, A., Lauerwald, R., Calle, L., Ichii, K., Anthoni, P., Arneth, A., Haverd, V., Jain, A. K., Kato, E., Kautz, M., Law, R. M., Lienert, S., Lombardozzi, D., Maki, T., Nakamura, T., Peylin, P., Rödenbeck, C., Zhuravlev, R., Saeki, T., Tian, H. Q., Zhu, D., and Ziehn, T.: State of the science in reconciling top-down and bottom-up approaches for terrestrial CO_2 budget, Glob Change Biol. 2020;26:1068–1084. https://doi.org/10.1111/gcb.14917, 2020

Liu, J., Bowman, K. W., Lee, M., Henze, D. K., Bousserez, N., Brix, H., Collatz, G. J., Menemenlis, D., Ott, L., Pawson, S., Jones D., and Nassar, R.: Carbon monitoring system flux estimation and attribution: impact of ACOS-GOSAT X_{CO2} sampling on the inference of terrestrial biospheric sources and sinks. Tellus B: Chemical and Physical Meteorology, 66(1). https://doi.org/10.3402/tellusb.v66.22486, 2014.

Liu, J., Bowman, K. W. and Lee, M.: Comparison between the Local Ensemble Transform Kalman Filter (LETKF) and 4D-Var in atmospheric CO_2 flux inversion with the Goddard Earth Observing System-Chem model and the observation impact diagnostics from the LETKF, J. Geophys. Res. Atmos., 121, 13,066–13,087, doi:10.1002/2016JD025100., 2016.

Liu, Z. Q., Zeng, N., Han, P. F., and Cai Q. X.: Impact of the horizontal resolution of GEOS-Chem on land–ocean and tropic–extratropic partitioning and seasonal cycle in CO_2 inversion, Environ. Res. Lett. 19 114007, 2024.

Lu, X., Jacob, D. J., Zhang, Y., Maasakkers, J. D., Sulprizio, M. P., Shen, L., Qu, Z., Scarpelli, T. R., Nesser, H., Yantosca, R. M., Sheng, J., Andrews, A., Parker, R. J., Boesch, H., Bloom, A. A., and Ma, S.: Global methane budget and trend, 2010–2017: complementarity of inverse analyses using in situ (GLOBALVIEWplus CH_4 ObsPack) and satellite (GOSAT) observations, Atmos. Chem. Phys., 21, 4637–4657, https://doi.org/10.5194/acp-21-4637-2021, 2021.

Maasakkers, J. D., Jacob, D. J., Sulprizio, M. P., Scarpelli, T. R., Nesser, H., Sheng, J.-X., Zhang, Y., Hersher, M., Bloom, A. A., Bowman, K. W., Worden, J. R., Janssens-Maenhout, G., and Parker, R. J.: Global distribution of methane emissions, emission trends, and OH concentrations and trends inferred from an inversion of GOSAT satellite data for 2010–2015, Atmos. Chem. Phys., 19, 7859–7881, https://doi.org/10.5194/acp-19-7859-2019, 2019.

Mathis, M., Lacroix, F., Hagemann, S., Nielsen D. M., Ilyina T., and Schrum, C.: Enhanced CO_2 uptake of the coastal ocean is dominated by biological carbon fixation. Nat. Clim. Chang. 14, 373–379 (2024). https://doi.org/10.1038/s41558-024-01956-w, 2024.

Meirink, J. F., Bergamaschi, P., and Krol, M. C.: Four-dimensional variational data assimilation for inverse modelling of atmospheric methane emissions: method and comparison with synthesis inversion, Atmos. Chem. Phys., 8, 6341–6353, https://doi.org/10.5194/acp-8-6341-2008, 2008.

Miller, S. M., Michalak, A. M., and Levi, P. J.: Atmospheric inverse modeling with known physical bounds: an example from trace gas emissions, Geosci. Model Dev., 7, 303–315, https://doi.org/10.5194/gmd-7-303-2014, 2014.

Nassar, R., Jones, D. B. A., Suntharalingam, P., Chen, J. M., Andres, R. J., Wecht, K. J., Yantosca, R. M., Kulawik, S. S., Bowman, K. W., Worden, J. R., Machida, T., and Matsueda, H.: Modeling global atmospheric CO_2 with improved emission

https://doi.org/10.5194/egusphere-2026-4830
Preprint. Discussion started: 20 August 2026

inventories and CO_2 production from the oxidation of other carbon species, Geosci. Model Dev., 3, 689–716, https://doi.org/10.5194/gmd-3-689-2010, 2010.

Niwa, Y., Ishijima, K., Ito, A. and Iida Y.: Toward a long-term atmospheric CO_2 inversion for elucidating natural carbon fluxes: technical notes of NISMON-CO_2 v2021.1. Prog Earth Planet Sci 9, 42 (2022). https://doi.org/10.1186/s40645-022-00502-6, 2022.

Oda, T. and Maksyutov, S.: A very high-resolution (1 km×1 km) global fossil fuel CO_2 emission inventory derived using a point source database and satellite observations of nighttime lights, Atmos. Chem. Phys., 11, 543–556, https://doi.org/10.5194/acp-11-543-2011, 2011.

Oda, T., Maksyutov, S., and Andres, R. J.: The Open-source Data Inventory for Anthropogenic CO_2, version 2016 (ODIAC2016): a global monthly fossil fuel CO_2 gridded emissions data product for tracer transport simulations and surface flux inversions, Earth Syst. Sci. Data, 10, 87–107, https://doi.org/10.5194/essd-10-87-2018, 2018.

O'Dell, C. W., Eldering, A., Wennberg, P. O., Crisp, D., Gunson, M. R., Fisher, B., Frankenberg, C., Kiel, M., Lindqvist, H., Mandrake, L., Merrelli, A., Natraj, V., Nelson, R. R., Osterman, G. B., Payne, V. H., Taylor, T. E. Wunch, D., Drouin, B. J., Oyafuso, F., Chang, A., McDuffie, J., Smyth, M., Baker, D. F., Basu, S., Chevallier, F., Crowell, S. M. R., Feng, L., Palmer, P. I., Dubey, M., García, O. E., Griffith, D. W. T., Hase, F., Iraci, L. T., Kivi, R., Morino, I., Notholt, J., Ohyama, H., Petri, C., Roehl, C. M., Sha, M. K., Strong, K., Sussmann, R., Te, Y., Uchino, O., and Velazco, V. A.: Improved retrievals of carbon dioxide from Orbiting Carbon Observatory-2 with the version 8 ACOS algorithm, Atmos. Meas. Tech., 11, 6539–6576, https://doi.org/10.5194/amt-11-6539-2018, 2018.

Parazoo, N.C., Bowman, K., Fisher, J. B., Frankenberg, C., Jones, D.B.A., Cescatti, A., Pérez-Priego, Ó., Wohlfahrt, G. and Montagnani, L.: Terrestrial gross primary production inferred from satellite fluorescence and vegetation models, Glob Change Biol, 20: 3103-3121. https://doi.org/10.1111/gcb.12652, 2014.

Pickett-Heaps, C. A., Rayner, P. J., Law, R. M., Ciais, P., Patra, P. K., Bousquet, P., Peylin, P., Maksyutov, S., Marshall, J., Rödenbeck, C., Langenfelds, R. L., Steele, L. P., Francey, R. J., Tans, P., and Sweeney, C.: Atmospheric CO_2 inversion validation using vertical profile measurements: Analysis of four independent inversion models, J. Geophys. Res., 116, D12305, doi:10.1029/2010JD014887., 2011.

Polavarapu, S., Dept. of Physics, University of Toronto, Lecture note: https://www.atmosp.physics.utoronto.ca/PHY2509/ch7.pdf, 2004.

Qu, Z., Jacob, D. J., Shen, L., Lu, X., Zhang, Y., Scarpelli, T. R., Nesser, H., Sulprizio, M. P., Maasakkers, J. D., Bloom, A. A., Worden, J. R., Parker, R. J., and Delgado, A. L.: Global distribution of methane emissions: a comparative inverse analysis of observations from the TROPOMI and GOSAT satellite instruments, Atmos. Chem. Phys., 21, 14159–14175, https://doi.org/10.5194/acp-21-14159-2021, 2021.

Shen, L., Jacob, D. J., Gautam, R., Omara, M., Scarpelli, T. R., Alba Lorente, A., Zavala-Araiza, D., Lu, X., Chen Z. C., and Lin J. T.: National quantifications of methane emissions from fuel exploitation using high resolution inversions of satellite observations, Nat Commun 14, 4948 (2023). https://doi.org/10.1038/s41467-023-40671-6, 2023.

Simone, N. W., Stettler, M. E. J., and Barrett, S. R. H.: Rapid estimation of global civil aviation emissions with uncertainty quantification, Trans. Res. Pt. D, 25, 33–41, https://doi.org/10.1016/j.trd.2013.07.001, 2013.

Stettler, M. E. J., Eastham, S., and Barrett, S. R. H.: Air quality and public health impacts of UK airports. Part I: Emissions, Atmospheric Environment, 45, 31, 2011, 5415-5424, https://doi.org/10.1016/j.atmosenv.2011.07.012, 2011.

Takahashi, T., Sutherland, S. C., Wanninkhof, R., Sweeney, C., Feely, R. A., Chipman, D. W., Hales, B., Friederich, G., Chavez, F., Sabine, C., Watson, A., Bakker, D. C. E., Ute Schuster, U., Metzl, N., Yoshikawa-Inoue, H., Ishii, M., Midorikawa,T., Nojiri, Y., Körtzinger, A., Steinhoff, T., Hoppema, M., Olafsson, J., Arnarson, T. S., Tilbrook, B., Johannessen, T., Olsen, A., Bellerby, R., Wong, C. S., Delille, B., N.R. Bates, N. R., and de Baar, H. J. W.: Climatological mean and decadal change in surface ocean pCO_2, and net sea–air CO_2 flux over the global oceans, Deep Sea Research Part II: Topical Studies in Oceanograph Volume 56, Issues 8–10, 2009, Pages 554-577, ISSN 0967-0645, https://doi.org/10.1016/j.dsr2.2008.12.009, 2009.

Teoh, R., Engberg, Z., Shapiro, M., Dray, L., and Stettler, M. E. J.: The high-resolution Global Aviation emissions Inventory based on ADS-B (GAIA) for 2019–2021, Atmos. Chem. Phys., 24, 725–744, https://doi.org/10.5194/acp-24-725-2024, 2024.

USA symposium report, The Goddard Earth Observing System 5 (GEOS-5) Model and Its Application to the Climate Research, APEC Climate Symposium, Lima, Peru, 19-21 August 2008, https://mddb.apec.org/documents/2008/ISTWG/SYM1/08_istwg_sym1_023.pdf, 2008.

Varon, D. J., Jacob, D. J., Sulprizio, M., Estrada, L. A., Downs, W. B., Shen, L., Hancock, S. E., Nesser, H., Qu, Z., Penn, E., Chen, Z., Lu, X., Lorente, A., Tewari, A., and Randles, C. A.: Integrated Methane Inversion (IMI 1.0): a user-friendly, cloud-based facility for inferring high-resolution methane emissions from TROPOMI satellite observations, Geosci. Model Dev., 15, 5787–5805, https://doi.org/10.5194/gmd-15-5787-2022, 2022.

van der Werf, G. R., Randerson, J. T., Giglio, L., Collatz, G. J., Mu, M., Kasibhatla, P. S., Morton, D. C., DeFries, R. S., Jin, Y., and van Leeuwen, T. T.: Global fire emissions and the contribution of deforestation, savanna, forest, agricultural, and peat fires (1997–2009), Atmos. Chem. Phys., 10, 11707–11735, https://doi.org/10.5194/acp-10-11707-2010, 2010.

https://doi.org/10.5194/egusphere-2026-4830
Preprint. Discussion started: 20 August 2026

Wang, H. M., Jiang, F., Liu, Y., Yang, D. X., Wu, M. S., He, W., Wang, J., Wang, J., Ju, W. M., and Chen, J. M.: Global Terrestrial Ecosystem Carbon Flux Inferred from TanSat XCO_2 Retrievals, J Remote Sens. 2022;2022:DOI:10.34133/2022/9816536, 2022.

Worden, J. R., Cusworth, D. H., Qu, Z., Yin, Y., Zhang, Y., Bloom, A. A., Ma, S., Byrne, B. K., Scarpelli, T., Maasakkers, J. D., Crisp, D., Duren, R., and Jacob, D. J.: The 2019 methane budget and uncertainties at 1° resolution and each country through Bayesian integration Of GOSAT total column methane data and a priori inventory estimates, Atmos. Chem. Phys., 22, 6811–6841, https://doi.org/10.5194/acp-22-6811-2022, 2022.

Wunch, D., Wennberg, P. O., Osterman, G., Fisher, B., Naylor, B., Roehl, C. M., O'Dell, C., Mandrake, L., Viatte, C., Kiel, M., Griffith, D. W. T., Deutscher, N. M., Velazco, V. A., Notholt, J., Warneke, T., Petri, C., De Maziere, M., Sha, M. K., Sussmann, R., Rettinger, M., Pollard, D., Robinson, J., Morino, I., Uchino, O., Hase, F., Blumenstock, T., Feist, D. G., Arnold, S. G., Strong, K., Mendonca, J., Kivi, R., Heikkinen, P., Iraci, L., Podolske, J., Hillyard, P. W., Kawakami, S., Dubey, M. K., Parker, H. A., Sepulveda, E., García, O. E., Te, Y., Jeseck, P., Gunson, M. R., Crisp, D., and Eldering, A., Comparisons of the Orbiting Carbon Observatory-2 (OCO-2) XCO_2 measurements with TCCON, Atmos. Meas. Tech., 10, 2209–2238, https://doi.org/10.5194/amt-10-2209-2017, 2017.